

**Best Available
Copy
for all Pictures**

12

RADC-TR-75-231
Final Technical Report
September 1975



DAYTIME ATMOSPHERIC TRANSFER FUNCTION STUDY
(DAYTIME SEEING STUDY)

Lockheed Palo Alto Research Labs

Sponsored by
Defense Advanced Research Projects Agency
ARPA Order No. 2646

Approved for public release;
distribution unlimited.

D D C
RECEIVED
SEP 9 1975
RACALU 150

The views and conclusions contained in this document are those of the authors and should not be interpreted as necessarily representing the official policies, either expressed or implied, of the Defense Advanced Research Projects Agency or the U. S. Government.

Rome Air Development Center
Air Force Systems Command
Griffiss Air Force Base, New York 13441

ADA018139

100

This report has been reviewed by the RADC Information Office (OI) and is releasable to the National Technical Information Service (NTIS). At NTIS it will be releasable to the general public including foreign nations.

This report has been reviewed and is approved for publication.

APPROVED:

Donald W. Hanson

DONALD W. HANSON

Project Engineer

ACCESSION FOR	
NTIS	White Section <input checked="" type="checkbox"/>
DDC	Buff Section <input type="checkbox"/>
UNANNOUNCED	
JUSTIFICATION	
BY	
DISTRIBUTION/AVAILABILITY NOTES	
DATE	REVIEW DATE
A	

Do not return this copy. Retain or destroy.

DAYTIME ATMOSPHERIC TRANSFER FUNCTION STUDY
(DAYTIME SEEING STUDY)

Alan M. Title

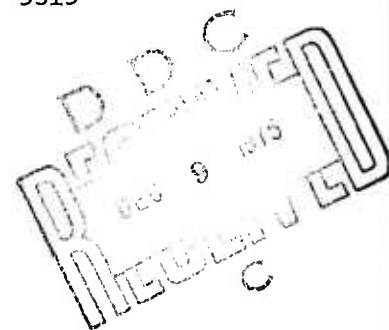
Contractor: Lockheed Palo Alto Research Labs
Contract Number: F30602-74-C-0144
Effective Date of Contract: 14 May 1974
Contract Expiration Date: 15 May 1975
Amount of Contract: \$65,000.00
Program Code Number: 5E20
Period of work covered: 15 Feb 74 - 15 Jun 75

Principal Investigator: Dr. Alan M. Title
415 493-4411, ext. 5315

Project Engineer: Donald W. Hanson
315 330-3144

Approved for public release;
distribution unlimited.

This research was supported by the Defense
Advanced Research Projects Agency of the
Department of Defense and was monitored by
Donald W. Hanson, RADC (OCSF), Griffiss
Air Force Base, New York 13441.



UNCLASSIFIED

SECURITY CLASSIFICATION OF THIS PAGE (When Data Entered)

REPORT DOCUMENTATION PAGE		READ INSTRUCTIONS BEFORE COMPLETING FORM
1. REPORT NUMBER RADC-TR-75-231	2. GOVT ACCESSION NO.	3. RECIPIENT'S CATALOG NUMBER
4. TITLE (and Subtitle) DAYTIME ATMOSPHERIC TRANSFER FUNCTION STUDY (DAYTIME SEEING STUDY)	5. TYPE OF REPORT & PERIOD COVERED Final Technical Report, 15 Feb 74 -- 15 Jun 75	6. PERFORMING ORG. REPORT NUMBER N/A
7. AUTHOR(s) Alan M./Title	8. CONTRACT OR GRANT NUMBER(s) F30602-74-C-0144, MARPA Order - 2646	9. PROGRAM ELEMENT, PROJECT, TASK AREA & WORK UNIT NUMBERS 62301E 26460301
10. PERFORMING ORGANIZATION NAME AND ADDRESS Lockheed Palo Alto Research Labs 3251 Hanover Street Palo Alto CA 94304	11. CONTROLLING OFFICE NAME AND ADDRESS Defense Advanced Research Projects Agency 1400 Wilson Blvd Arlington VA 22209	12. REPORT DATE September 1975
13. MONITORING AGENCY NAME & ADDRESS (if different from Controlling Office) Rome Air Development Center (OCSE) Griffiss AFB NY 13441	14. SECURITY CLASS. (of this report) N/A	15. NUMBER OF PAGES 44
16. DISTRIBUTION STATEMENT (of this Report) Approved for public release; distribution unlimited.		
17. DISTRIBUTION STATEMENT (of the abstract entered in Block 20, if different from Report) Same		
18. SUPPLEMENTARY NOTES RADC Project Engineer: Donald W. Hanson/OCSE		
19. KEY WORDS (Continue on reverse side if necessary and identify by block number) Optics Atmosphere Propagation Isoplanatic		
20. ABSTRACT (Continue on reverse side if necessary and identify by block number) It is of critical importance to know the temporal and spatial character of the isoplanatic patch, in order to access or design predetection compensation systems. A system which uses the edge of the sun as an extended target in order to determine the daytime spatial and temporal characteristics of the isoplanatic patch is described. Preliminary data gathered at the Rye Canyon Solar Observatory are presented.		

DD FORM 1 JAN 73 1473

EDITION OF 1 NOV 65 IS OBSOLETE

UNCLASSIFIED

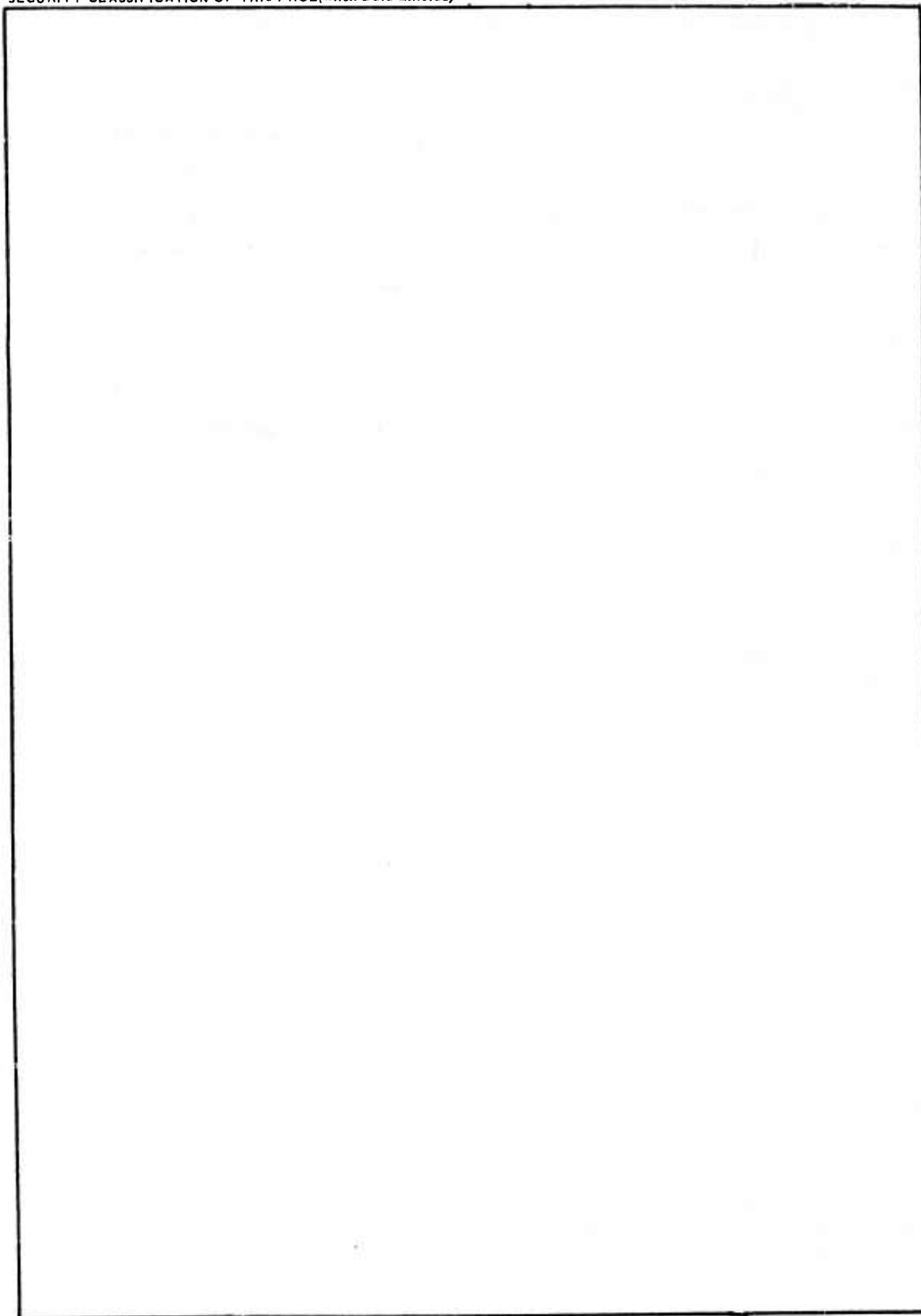
SECURITY CLASSIFICATION OF THIS PAGE (When Data Entered)

210118

VB

UNCLASSIFIED

SECURITY CLASSIFICATION OF THIS PAGE(When Data Entered)



UNCLASSIFIED

SECURITY CLASSIFICATION OF THIS PAGE(When Data Entered)

ABSTRACT

It is of critical importance to know the temporal and spatial character of the isoplanatic patch, in order to access or design pre- or post-detection systems. Here, we report on progress on a system that uses the edge of the sun as an extended target in order to determine the daytime spatial and temporal characteristics of the isoplanatic patch.

Preliminary measurements at the Rye Canyon site indicate a greater than 50% probability that two points separated by 10 arc seconds are in the same isoplanatic patch. The data also indicates that when the 10 arc second conditions do not exist that the maximum separation for the same isoplanatic patch is 2 to 3 arc seconds.

The measurement uses a pair of linear diode arrays that are aligned along solar radii at points that cross the image of the edge. A description of the telescope and the array electronics is included.

TABLE OF CONTENTS

	<u>Page</u>
ABSTRACT	iv
INTRODUCTION	1
OPTICAL INSTRUMENTATION	4
TELESCOPE OPTICAL CHARACTERISTICS	9
ELECTRONIC INSTRUMENTATION	10
DATA HANDLING PROCEDURE	16
RESULTS	18
CONCLUSIONS	20
APPENDIX	21

TABLE LIST

	Page
Table 1. Explanation of Optical Schematic Notations in Figure 2	6
Table 2. Optical Characteristics of 12-inch Telescope	9
Table 3. RMS Limb Excursion (Arc Seconds)	23

LIST OF FIGURES

Figure 1. Photograph of 12-inch Telescope	5
Figure 2. Optical Schematic of 12-inch Telescope	6
Figure 3. Photograph of side of 12-inch Telescope, showing inside view	7
Figure 4. Photograph of back end of 12-inch Telescope, showing beam exit windows	8
Figure 5. Block diagram of electronic instrumentation	11
Figure 6. Photograph of diode arrays, close up view, and beam splitter	12
Figure 7. Photograph of diode array housing	13
Figure 8. Photograph of circuitry inside main control cabinet	14
Figure 9. Photograph of main control cabinet	15

INTRODUCTION

The central problems of visible space object identification are the elimination of the disturbances to a telescopic image introduced by the atmosphere and the achievement of diffraction limited performance.

In the mid-60s, Joseph Goodman demonstrated that aperture plane correction could remove the effects of a random atmosphere if the atmosphere was sufficiently close to the telescope, (Goodman, J. W., "Restoration of Atmospherically Degraded Images, A Woods Hole Summer Study," July 1966). Since then, there has been a great deal of progress. A group at Itek has demonstrated an active aperture control system that can correct a random atmosphere created by a heat source, given a suitable reference signal. It is clear that the Itek technique can be extended to perform the aperture correction for a large telescope, and that if the random atmosphere satisfies the condition that it is sufficiently close to the aperture plane, diffraction-limited performance can be achieved.

The critical questions then reduce to the actual behavior of the atmosphere and the method of generating or the method of deriving a reference signal.

The diffraction-limited imaging program has two major requirements;

- o To correct the atmospheric point spread function in real time, which requires real time detection of the atmospheric point spread function.
- o To obtain and quantify the diffraction-limited images in a useful form, requiring detecting, recording, storing, and processing of the diffraction-limited images.

In order to attack requirement number one in an efficient manner, the effect of limitations placed upon the correction system by the atmosphere must be understood. Since the early '60s, a large number of scientists have been analytically attacking the problem of propagation through a turbulent atmosphere. Mathematically, the general transfer problem is stated as

$$I'(\zeta, \eta) = \int_A \int dx dy I(x, y) P(x, y, \zeta, \eta) \quad (1)$$

where $I(x, y)$ is the perfect image, $I'(\zeta, \eta)$ is the detected image, $P(x, y, \zeta, \eta)$ is the point spread function, and A is the area of the image. In general, as indicated in equation (1), the PSF will vary from point to point in the image plane. If equation (1) is written in discrete form:

$$I'_{mn} = \sum_{i=1}^M \sum_{j=1}^M I_{ij} P_{ijmn}, \quad (2)$$

where the real and detected images are described by an $M \times M$ matrix and the point spread function is described by M^4 matrix.

Computationally, the general problem is extremely difficult to solve and most efforts in image transfer problems have attacked

$$I'(\zeta, \eta) = \int_A \int dx dy I(x, y) P(\zeta - x, \eta - y) \quad (3)$$

The point spread function indicated in equation (3) retains its analytic form over the entire image. It is called the spatially invariant point spread function (SIPSF). If the transfer problem is the atmospheric transfer problem, the area, A , over which equation (3) is valid is called the isoplanatic patch.

A great deal of mathematical expertise on propagation through a random medium has been built up, unfortunately, however, an equally impressive amount of experimental results are not available. In particular, it is not known over how large an angle in the sky the atmospheric PSF is the same, that is, the size of the object, and hence the image, over which the short term point spread function is space invariant (STSIPSF). Further, since the STSIPSF region size is not known, the time over which a single realization of the STSIPSF exists is not known precisely. However, it is known that the time scale is not much longer than 1/50 second and the angular scale is not

much smaller than 2 arc seconds.

The work we are doing attempts to measure the size of the isoplanatic patch by studying the difference between the intensities recorded from pairs of detectors aligned using solar radii at positions that cross the limb. By varying the angle between the radii data from angles up to 32 minutes of arc can be compared. Exposures can be recorded and repeated within 3×10^{-3} seconds. The detectors are 256 element linear diode arrays. Hence, the detector geometry is fixed.

In the sections below the design of the telescope, the design of the electronics, the experimental and data reduction procedures, and our initial conclusions are discussed. Also included is a large appendix containing data at various processing stages, data processed by different techniques, and statistical measures of some data runs.

Optical Instrumentation

The telescope designed and constructed for this study is a 12-inch folded refractor. The 12-inch diameter objective lens has a focal length of 168 inches. In order to achieve diffraction limited results, the surfaces of the BK-7 Schlieren quality Grade A glass, are aspheric. In order to keep temperature induced focus shifts and obtain the highest image contrast, it was decided to use a single lens objective. Since a single lens objective is uncorrected for chromatic aberration, that is to say all colors do not come to the same focus, a monochromatic image was obtained with a 30 angstrom half bandwidth filter. The telescope's primary focal length of 168 inches produces a solar image of approximately 1.6 inches which can be increased as much as 5 times with secondary enlarging optics.

Figure 1 is a photograph of the 12-inch telescope used in this experiment. The main body of the telescope is aluminum plate, the outside of which is coated with a paint containing a high proportion of white titanium dioxide pigment for maximum reflection of incident sunlight. This paint helps to minimize internal telescope heating which can deteriorate optical performance. It can be seen by the nature of this experiment that negligible seeing effects inside the telescope housing must be maintained.

All interior surfaces are lined with polyurethane insulation and the 30-inch snout, projecting from the front of the main body, which contains the objective lens, is further insulated on its outside surface with a second layer of polyurethane, and this covered with an aluminum housing. The front of the main body is shielded from direct sunlight by a thin sheet of aluminum mounted on 2-inch plastic standoffs.



Figure I . Photograph of 12-inch telescope.

In order to keep the length of the telescope manageable, the optical path is folded by two 8-inch mirrors, designated M_1 and M_2 . Folding the telescope decreases its total length from nearly 18 feet to a far more manageable 10.5 feet. The main optical beam can be further diverted by mirrors M_3 and M_4 (Figure 2) to an auxiliary position. The auxiliary position increases the flexibility of the system by providing a possible test bed for experimentation and instrumentation development.

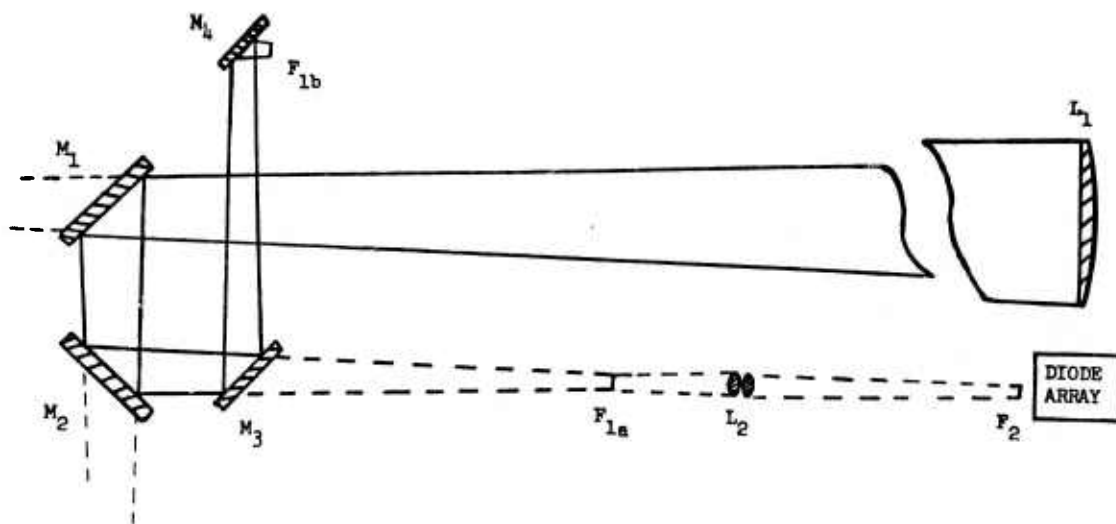


Figure 2 . Optical schematic of 12-inch telescope.

Table I . EXPLANATION OF NOTATIONS IN FIGURE

L_1	12-inch diameter objective lens with a 168 inch focal length
L_2	Enlarging lens, $5 \frac{3}{4}$ -inch focal length can enlarge primary image 2 to 5 times
F_{1a}	Primary focus position
F_2	Enlarged image position at which diode array will be placed
F_{1b}	Auxiliary beam primary focus position
M_1	First beam folding flat mirror 8-inch diameter. Front surface has dielectric coating which reflects useful wavelengths and allows much of the non-useful radiant energy to pass.
M_2	Second beam folding flat mirror 8-inch diameter, coating same as M_1 .
M_3	Third beam folding mirror 6-inch diameter can be flipped 45° .

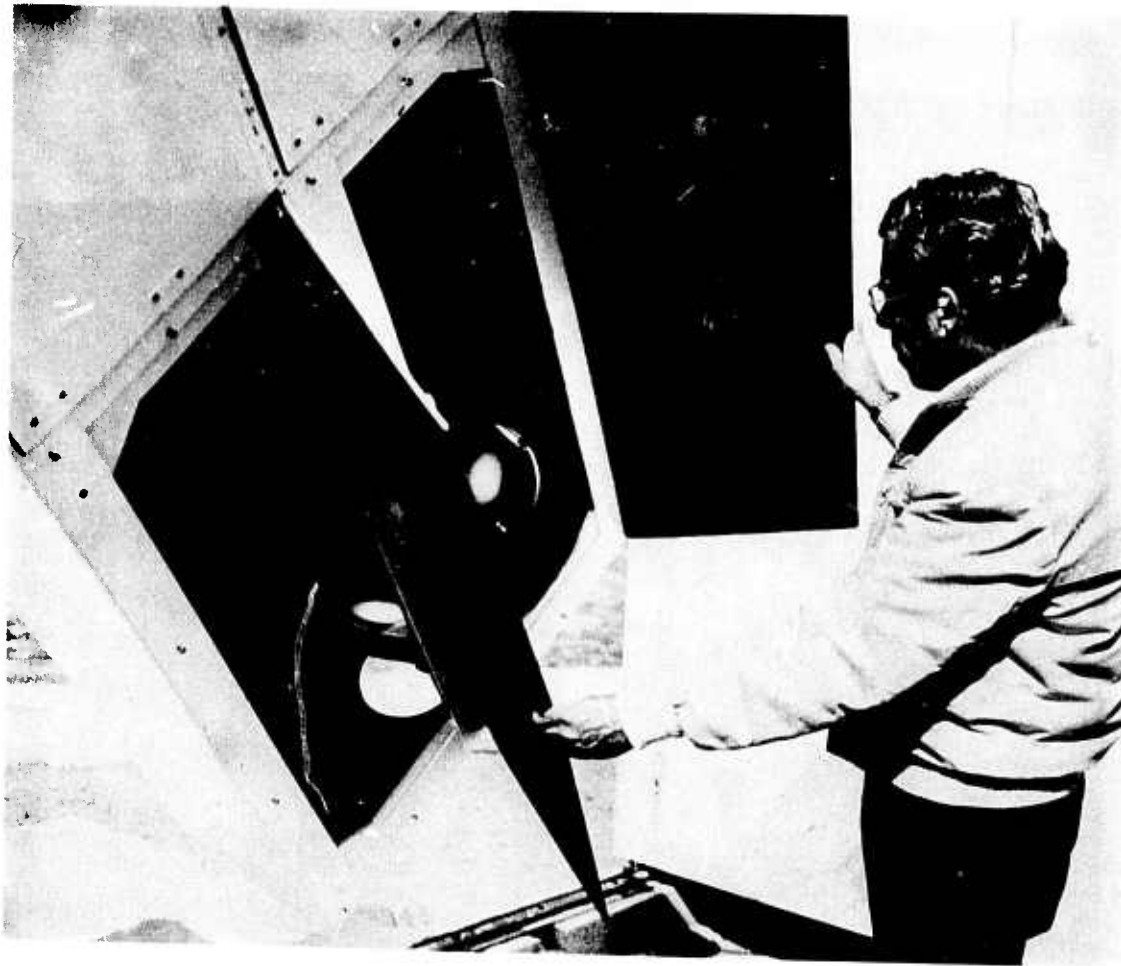


Figure 3 . Photograph showing interior of telescope.

Since a major source of image distortion is the hot solar beam itself, a large portion of this radiant energy will be passed right through the telescope by means of a dielectric coating on the first and second mirrors (M_1 and M_2). Useful wavelengths will be reflected to the diode array and as much unwanted radiation as possible will pass through M_1 and M_2 out the back of the telescope. These two mirrors can be seen in the above figure, along with one of the exit windows.

Four doors, two of which are open in the photograph, give complete accessibility to the interior of the telescope.

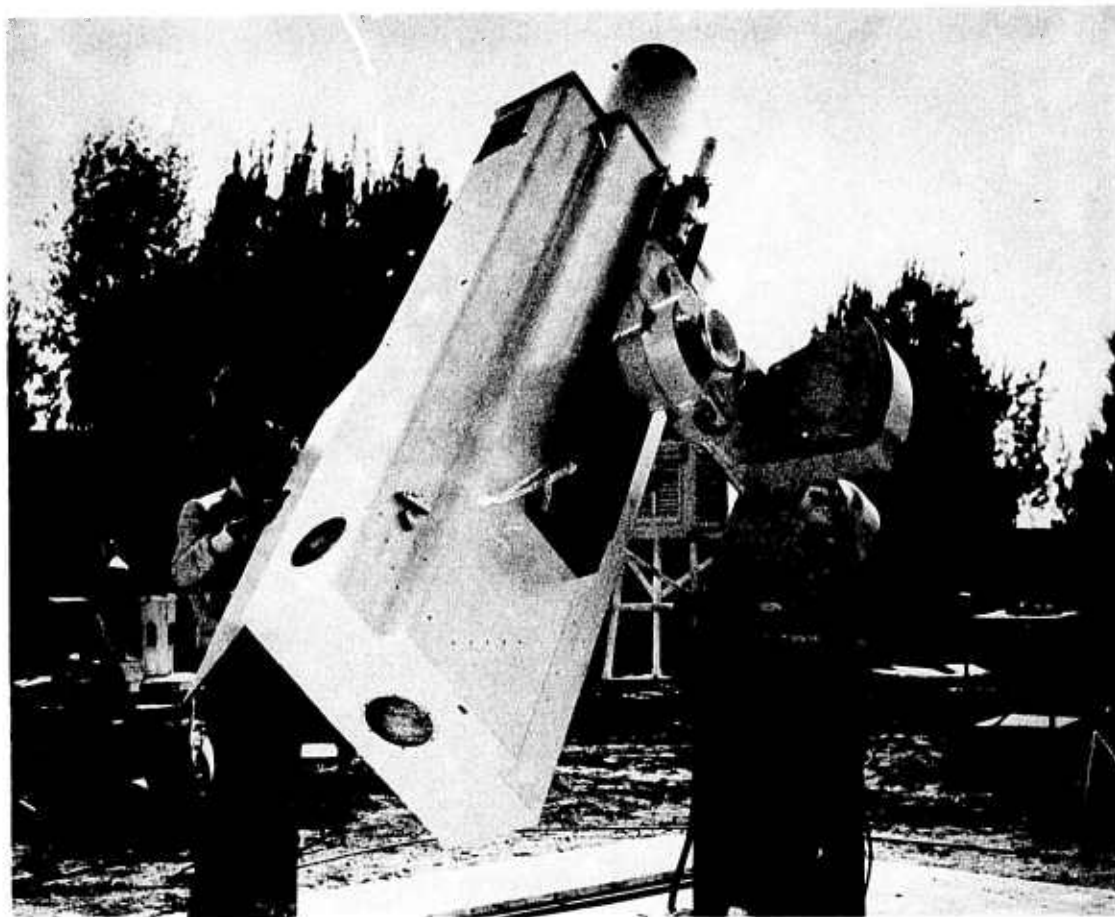


Figure 4 . Photograph showing the back end of the 12-inch telescope. The two beam exit windows can be seen in the lower left. The windows are made of plexiglass.

To further segregate the optical beam from any cross currents inside the main body, a 12-inch diameter cardboard tube encompasses the beam most of the way to the first fold mirror (M_1).

Telescope Optical Characteristics

Some of the basic telescope optical characteristics are given in Table 2, along with the image scale and effective focal ratio obtained with image magnification ranging from 1 to 5. Since several diode arrays, consisting of 256 individual silicon elements each approximately 0.001-inch square, will be used in this study, image scale in Table 2 is given in seconds of arc per 0.001 inch.

TABLE 2

Telescope Objective: 12-inch Diameter Aspheric Singlet
Focal Length: 168.5 inches
Focal Ratio: f/14
Primary image scale: 1224 seconds of arc per inch

<u>Magnification of Prime Image</u>	<u>Effective Focal Ratio</u>	<u>Image Scale in Second of Arc per Diode Array Element *</u>
1.0	14	1.22
1.5	21	0.82
2.0	28	0.61
2.5 +	35	0.49
3.0	42	0.41
3.5	49	0.35
4.0	56	0.31
4.5	63	0.27
5.0	70	0.24

* .001 inch

+ Magnification used in this study

Electronic Instrumentation

The electronics for this experiment can be conveniently viewed as consisting of four parts: (1) sensor, (2) signal processor, (3) control logic, and (4) interface. Figure 5 is a block diagram of the electronic instrumentation.

There are two sensors, each consisting of a 256 element photodiode array, associated drive circuitry, and an output amplifier mounted on a single small circuit board (Figure 6). These circuit boards, together with a third board containing clock generating circuitry are fastened to the beam splitter and mounted inside the telescope (Figure 7). The output of each sensor is a series of analog pulses which is fed via shielded cable to the signal processor.

The signal processor consists of five large circuit boards together with associated power supplies (Figure 8) mounted in a small cabinet (Figure 9) and located immediately adjacent to the telescope. In the signal processor, each pulse is sampled at its beginning and at its peak by very high speed sample and holds. The outputs of these sample and holds are fed into differential amplifiers and thus produce an analog signal proportional to the amplitude of the pulses but relatively insensitive to noise at the input. At this point, the analog signals are converted by a pair of high speed analog to digital converters into 10 bit words. These digital words are then clocked into a mos memory.

In the same location as the signal processor, is a sixth large circuit board containing the control logic. This board, consisting of a mixture of ordinary and high speed TTL logic, provides the proper timing signal to the other parts of the system.

The interface circuitry, located partly adjacent to the signal processor and partly adjacent to the computer, takes each 10 bit word, converts it to serial data, and sends it via coaxial cable to the computer. At the computer, the data is converted back into parallel form and fed directly into memory via a DR-11B direct memory access.

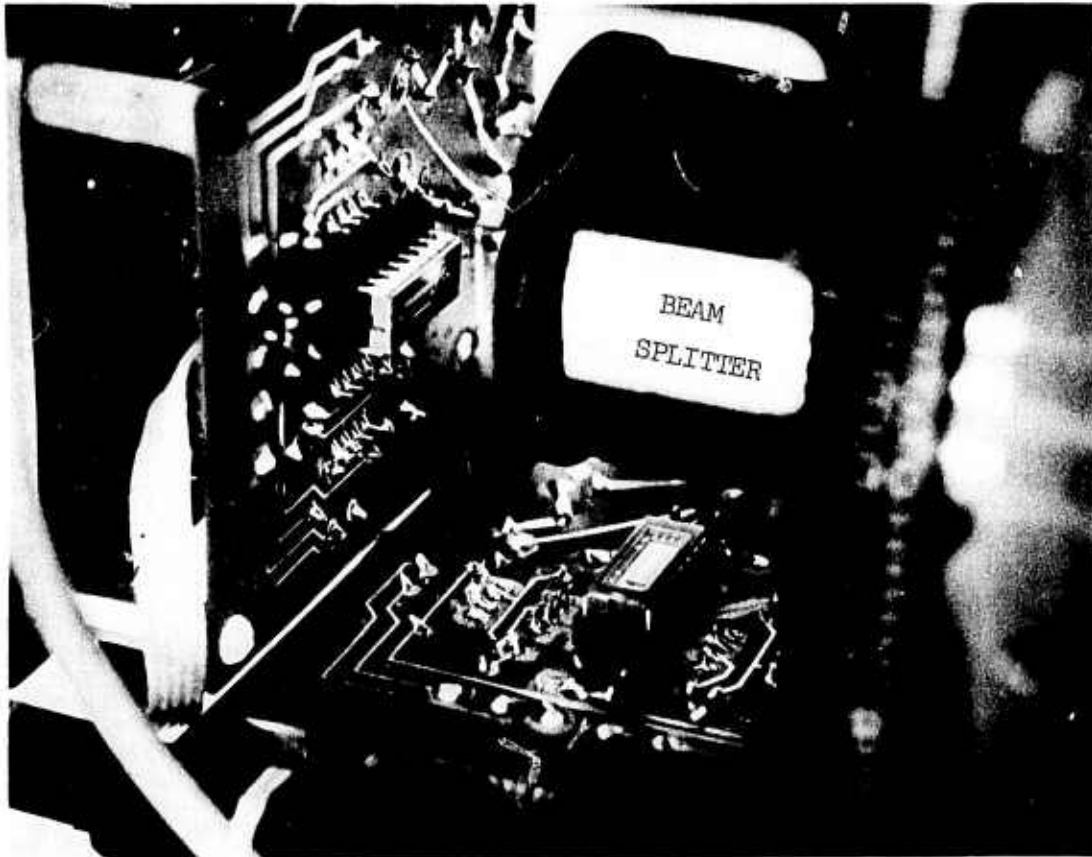


Figure 6 . Photograph of two diode arrays, and their associated circuitry. One diode array remains stationary, while the other one is moveable so as to make variable the sampling positions on the limb of the sun, from cospatial to many minutes of arc apart. The beam splitter (labeled) passes 50% of the light straight through to one diode array and 50% of the light is reflected at 90° to the other diode array.

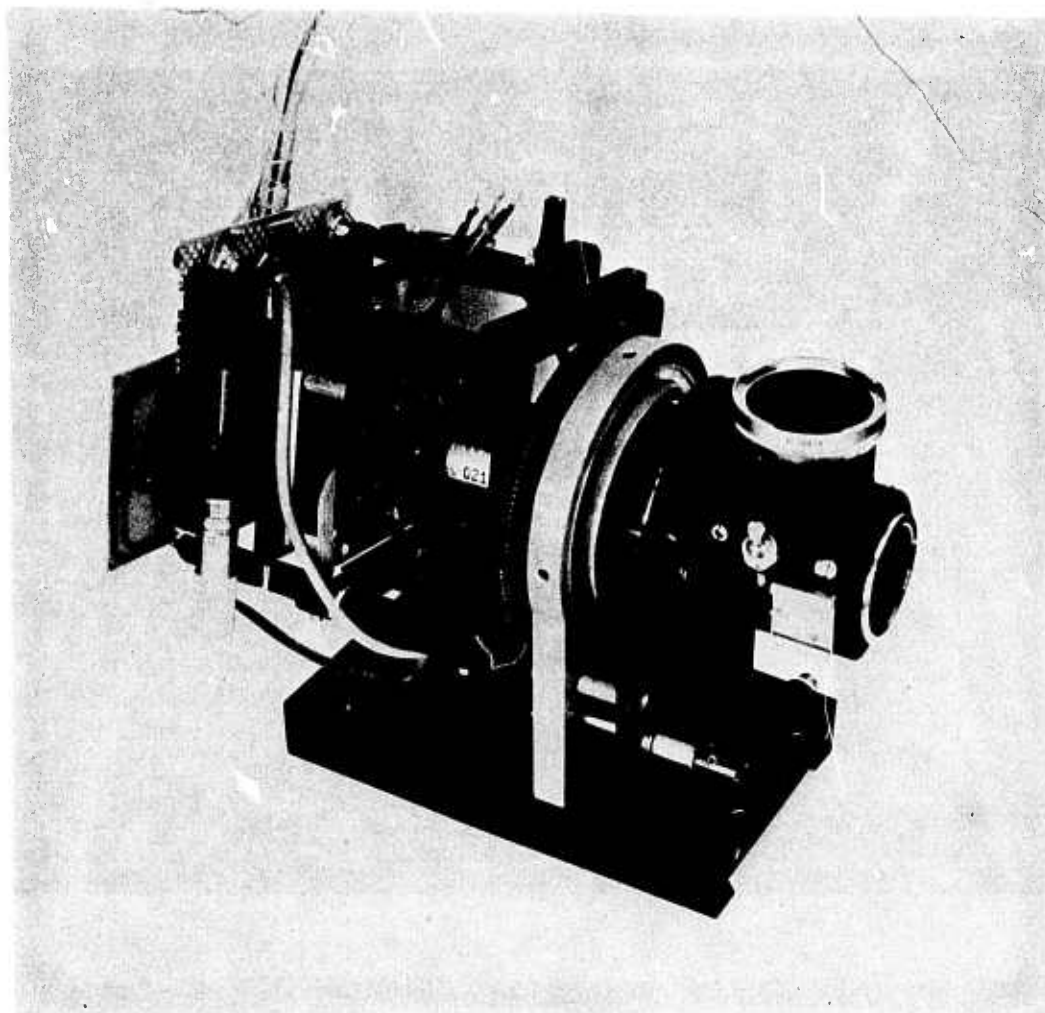


Figure 7 . Photograph of rotatable diode array housing. The front of the housing contains a Leica Visoflex unit for viewing and focusing the image, by means of a flip mirror. On the back of the housing can be seen the micrometer, and stage, by which one of the diode arrays can be moved. In turn, both diode arrays can be rotated 360° .

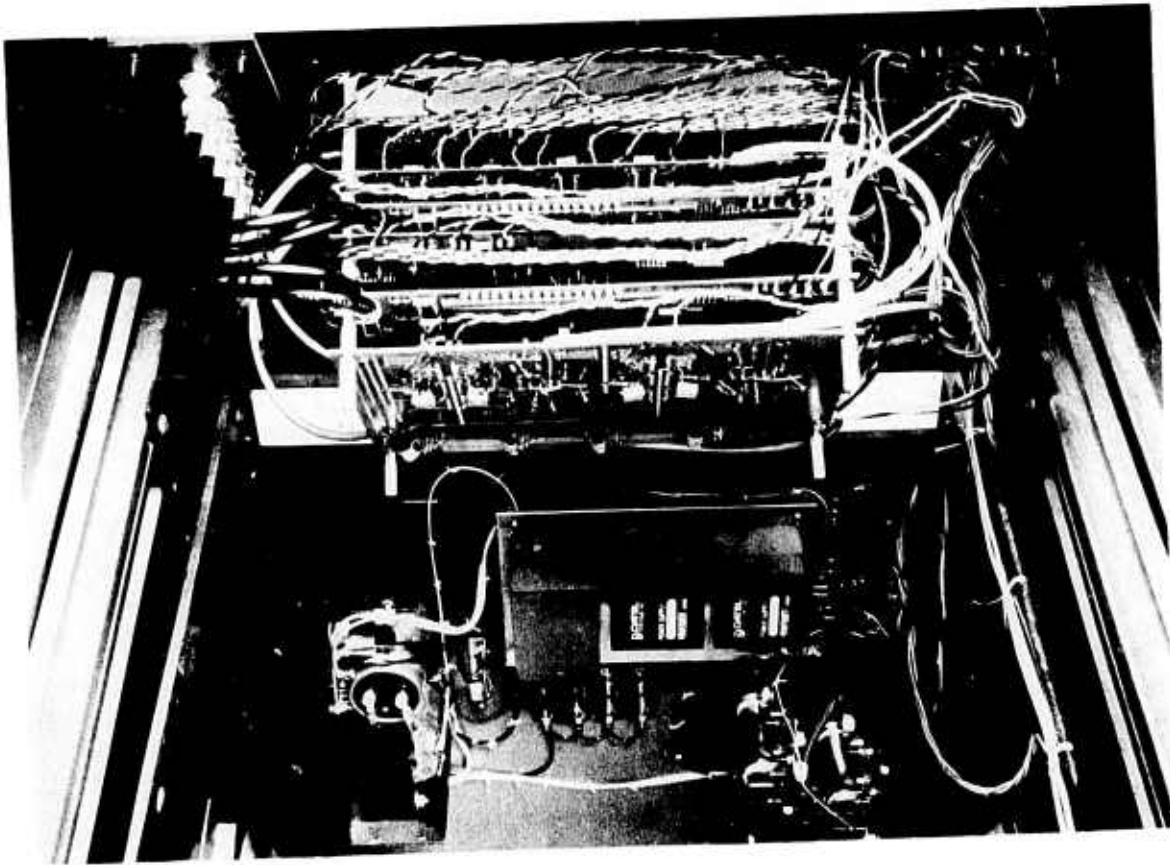


Figure 8. Photograph of circuit boards, and associated power supplies, inside cabinet in Figure 9. Most of the circuit boards contain the signal processor. Also contained in this cabinet is the control logic, consisting of ordinary and high speed TTL logic.

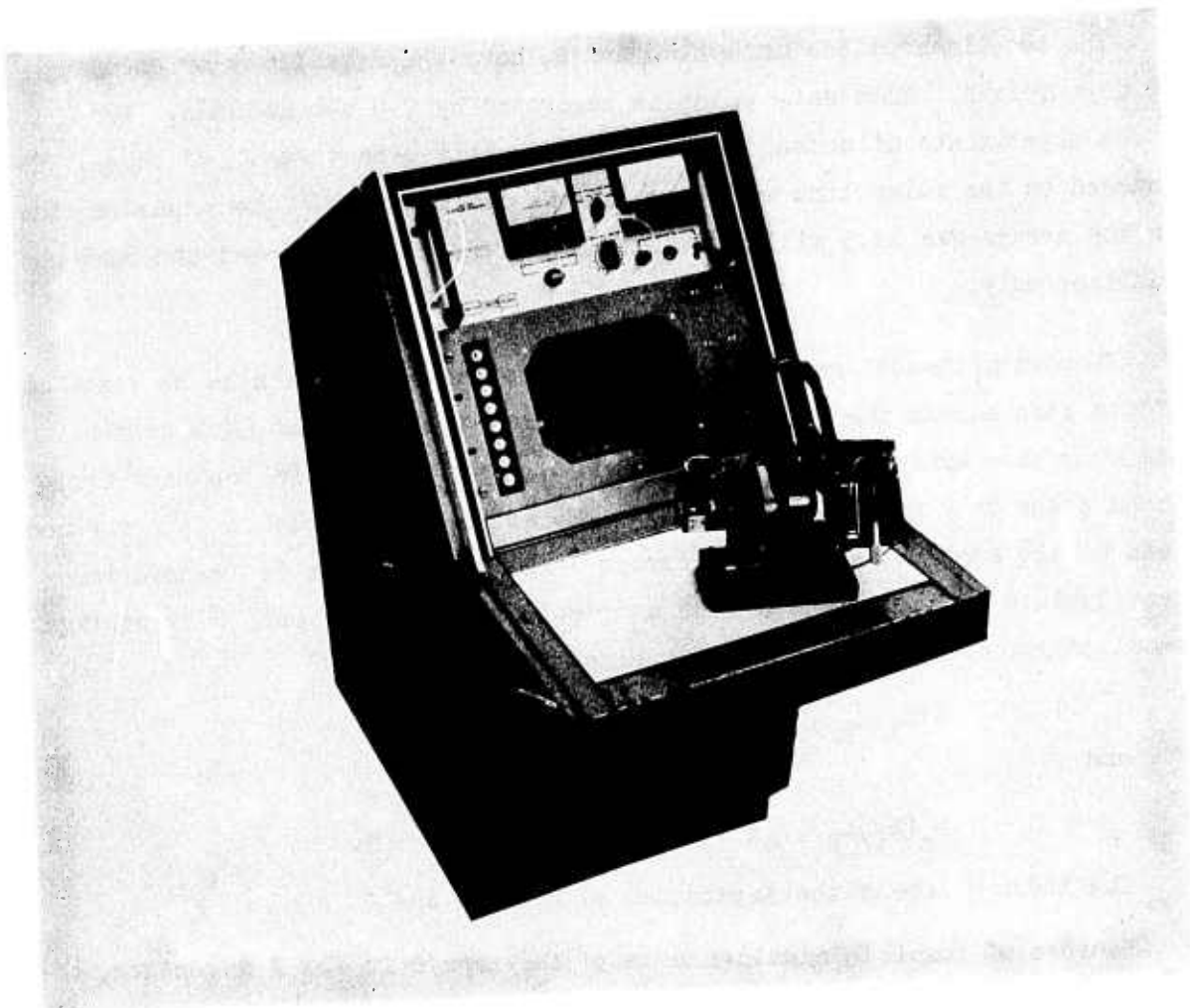


Figure 9 . Photograph of main control cabinet. This cabinet contains the signal processing electronics, along with the associated power supplies. On the control cabinet shelf can be seen the diode array housing. This housing is more clearly shown in Figures 6 and 7 .

Data Handling Procedures

The two linear diode arrays, A and B, have the capability of encoding 256 data points. Each data point is separated by 0.5 arc seconds. For all of the experiments discussed here, only 64 points were taken. Of these, 32 centered on the solar limb were used in the calculations. The exposure time for the arrays was 12.5 milliseconds. Both arrays were exposed and read out simultaneously.

Each experimental measurement of the isoplanatic patch size consists of 21 data runs across the sun's limb and 3 calibration runs at disk center. Data runs have array separations from 0 to 10 arc seconds in one half arc second steps or 0 to 20 arc seconds in one arc second steps. A data run consists of 128 successive reads of arrays A and B. The data is transferred directly into core and then at the completion of the run, onto disk storage. Symbolically, each run creates two arrays:

$$A(X_i, t_k), \quad i = 1, 64 \quad (4)$$

and

$$B_m(X_i, t_k), \quad k = 1, 128 \quad (5)$$

The index m labels the separation of array A and B.

Because of possible misalignments of the arrays in the X direction, the time averages.

$$\bar{A}(X_i) = \sum_{k=1}^{128} A(X_i, t_k) / 128 \quad (6)$$

$$\bar{B}_m(X_i) = \sum_{k=1}^{128} B_m(X_i, t_k) / 128 \quad (7)$$

are formed. Then the function

$$C_m(\Delta) = \sum_{i=c-10}^{i=c+10} \left[\bar{A}(X_i) - \bar{B}_m(X_i + \Delta) \right]^2 \quad (8)$$

is minimized with respect to Δ . The value c is the mean limb center position. Because $C_m(\Delta)$ is minimized by discrete steps small systematic

error signals can occur. The B_m arrays are then renumbered such that

$$B'_m(X_i) = B_m(X_i + \Delta), \quad (9)$$

and both arrays are renumbered such that c-16 equals 1. The prime notation shall be dropped.

The fundamental distortion data is from the mean square difference functions

$$D_m^2(t_k) = \sum_{i=1}^{32} [A(X_i, t_k) - B_m(X_i, t_k)]^2 / 32 \quad (10)$$

In order to obtain consistent comparisons with the cross products function difference below

$$D_o^2 = \sum_{k=1}^{128} D_o^2(t_k) \quad (11)$$

is subtracted from $D_m^2(t_k)$

to form

$$\underline{D}_m^2(t_k) = D_m^2(t_k) - D_o^2 \quad (12)$$

The functions $\underline{D}_m^2(t_k)$ are the time varying mean square differences of A and B_m arrays at separation m. Included in appendix A are plots of $\underline{D}_m^2(t_k)$ for a number of experiments. In addition to the \underline{D}_m^2 functions, a set of cross products

$$CP_m(t_k, n) = \sum_{i=1}^{32} [A(X_i, t_k) - B_m(X_i, t_k)] \quad (13)$$

$$\times [A(X_i, t_k + n) - B_m(X_i, t_k + n)]$$

are formed. The purpose of the cross product functions are to demonstrate the true decorrelation of the difference functions. Several sets of cross product functions are shown in the appendix A.

In order to get an idea of angle of arrival and image sharpness some additional functions are formed.

$$AB_m(t_k) = AC(t_k) - BC(t_k), \quad (14)$$

where $AC(t_k)$ and $BC(t_k)$ are respectively the limb center position of the A and B_m arrays at a particular time.

The functions $SA(t_k)$ and $SB_m(t_k)$ are the slopes at the limb centers of the arrays. The slopes are a least squares fit straight line to 5 points centered at the center limb point.

Results

Shown in Figure A1.1 is the difference data.

$$D_m(X_i, t_k) = A(X_i, t_k) - B_m(X_i, t_k) \quad (15)$$

for separations of 0, 2, 4, 6, 8, 10 arc seconds. It is apparent that the data takes on a different character for separations of 6 arc seconds and greater. Figure A1.2 is A1.1 slightly defocused to make the variations more visible. Shown in Figures A2.1 and A2.2 are $D_m^2(t_k)$ for experiment 7 (12 inch aperture 1/2 arc second steps). For separations greater than 10 (5 arc seconds) there are significant peaks in the mean square difference functions. The peaks are about 100 milliseconds wide. For separations less than $m = 10$ all of the records except 2, 3 and 4 are essentially identical to the zero separation. Experiment 7 seems to indicate that there is a 1 in 3 chance that 2 points separated by five arc seconds will suffer the same distortion.

In order to calibrate the records a mean square difference in calibration was formed.

$$D_{cal}^2 = \sum_{i=1}^{32} \left[A(X_i) - \underline{A}(X_i + 1) \right]^2 \quad (16)$$

Since a displacement of a single point corresponds to an image displacement of 0.5 arc second, D_{cal}^2 is the mean signal that will occur when the images on arrays A and B have a relative displacement of 0.5 arc seconds. On all figures that show difference and cross product functions D_{cal}^2 is half full scale; that is, half the separation between adjacent zero lines. The data in Figure A2.1 separation zero is essentially system noise. The maximum deflections on this trace correspond to displacements of less than 0.1 arc second.

Shown in Figures A3.1 and A3.2 are the distribution functions for the limb center slope for each of the runs. It is interesting to note that run 2 shows a significantly different slope distribution function. Fried has shown that there is relationship between the size of r_0 and the chance of obtaining an undistorted image point (unpublished). Hence, this data seems to indicate that

there can arise significant variations of r_0 on time scales required to change the array separation which is about one minute. Shown in Figures A3.3 and A3.4 are time variations of the limb slopes for array A.

In order to quantify the magnitude of mean square difference function excursions the number of occasions the mean square difference exceeded multiples of the standard deviation of $D_0^2(t)$ was calculated. Shown in Figure A3.5 are histograms of excursion counts versus mean number for one, two, and three standard deviations.

Shown in Figures A4.1 through A4.10 are cross product functions for 12.5, 25, 50, 100, and 200 milliseconds. A comparison with A2.1 and A2.2 shows that the cross product functions are essentially the same as the mean square difference functions for 12.5 milliseconds, but differ significantly after 50 milliseconds. For separations of less than 5 arc seconds, see A4.9 lines 2 and 3, there is some correlation. These runs are those that exhibited displacement signals that lasted a long time as can be seen directly in A4.1. These runs also correspond to significant decorrelation at 2 arc second separation. Perhaps this suggests that whatever is causing the 2 second decorrelation has a different true scale than that which causes the 5 second decorrelation.

Conclusions

This experiment was designed as a feasibility study for measuring the daytime isoplanatic patch size. Based on the data now in hand it appears that, at least at the Rye Canyon site, two points with a separation of 5 arc seconds have a 1 in 3 chance of suffering the same distortion and relative displacement to an accuracy of 0.1 arc second.

This suggests that the low differential distortion is a factor of 2 greater in diameter than 5 arc seconds simply because if the region were only 5 arc seconds in diameter there would be a zero probability of two points with a 5 second separation being in the same region. There still exists a question that even if two points have the same distortion function, are they in the same isoplanatic patch in the predetection sense. However, at the very least this data indicates that the possibility exists that the patch size is 10 arc seconds. At the very worst it is clear that 10 arc seconds represents an upper bound in the patch size.

Shown in Figure A5.1 is a photograph of solar granulation at disk center with a ten arc second circle for comparison.

In those cases that a 10 arc second patch does not exist it appears that the patch size is on the order of 2 arc seconds. Evidence from the distribution of slope, which indicates the image sharpness variation, would seem to show that r_0 suddenly changes. Because both sharpness and patch size decrease simultaneously the disturbance must be occurring far from the telescope and is not the result of a sharp wind gust.

The cross product functions indicate that exposures can safely be made for times up to about 25 milliseconds or $1/40$ second. Exposure times of greater than 50 milliseconds are clearly marginal and 100 millisecond exposure will surely contain more than one realization of the isoplanatic patch.

Although Experiment 7 is discussed in great detail, 22 experiments have been run and reduced. Most of these have been done with the full 12" aperture

Several have been taken with a 4.75" aperture. Substantially the same character is shown by all the data. Shown in Table 3 is the root mean square limb excursion for seven experiments.

TABLE 3 - RMS LIMB EXCURSION (ARC SECONDS)

	EXPERIMENT NUMBER									
m	7	13	14	15	16	17	18	20	21	
0	.053	.049	.047	.036	.062	.047	.038	.103	.037	
1	.036	.039	.048	.035	.081	.050	.050	.098	.054	
2	.083	.059	.048	.049	.069	.065	.054	.087	.072	
3	.071	.072	.052	.056	.122	.071	.041	.121	.073	
4	.075	.075	.064	.070	.091	.077	.082	.134	.098	
5	.068	.091	.093	.065	.160	.078	.074	.137	.090	
6	.058	.112	.058	.085	.148	.122	.091	.133	.128	
7	.080	.119	.054	.073	.157	.111	.096	.135	.152	
8	.095	.118	.057	.080	.173	.103	.081	.152	.130	
9	.093	.101	.063	.114	.108	.108	.117	.221	.148	
10	.093	.136	.065	.086	.128	.140	.094	.155	.134	
11	.111	.137	.071	.101	.129	.135	.133	.152	.185	
12	.151	.162	.074	.092	.149	.130	.106	.214	.138	
13	.157	.170	.094	.096	.123	.133	.117	.151	.198	
14	.114	.193	.090	.114	.154	.140	.106	.217	.170	
15	.115	.191	.084	.114	.167	.111	.096	.219	.262	
16	.120	.200	.087	.084	.123	.169	.101	.220	.226	
17	.211	.226	.076	.075	.136	.125	.099	.232	.239	
18	.153	.291	.107	.129	.140	.152	.099	.197	.177	
19	.132	.229	.088	.128	.182	.140	.104	.158	.244	
20	.163	.193	.103	.111	.140	.183	.099	.228	.098	

NOTES: 1.) Experiments 16 and 17 were done with a 15 cm diameter aperture, all others used a 30 cm aperture.

2.) For Experiments 7, 13, and 14 the separation increment was 0.5 arc second, and others used one arc second separation increments.

APPENDIX

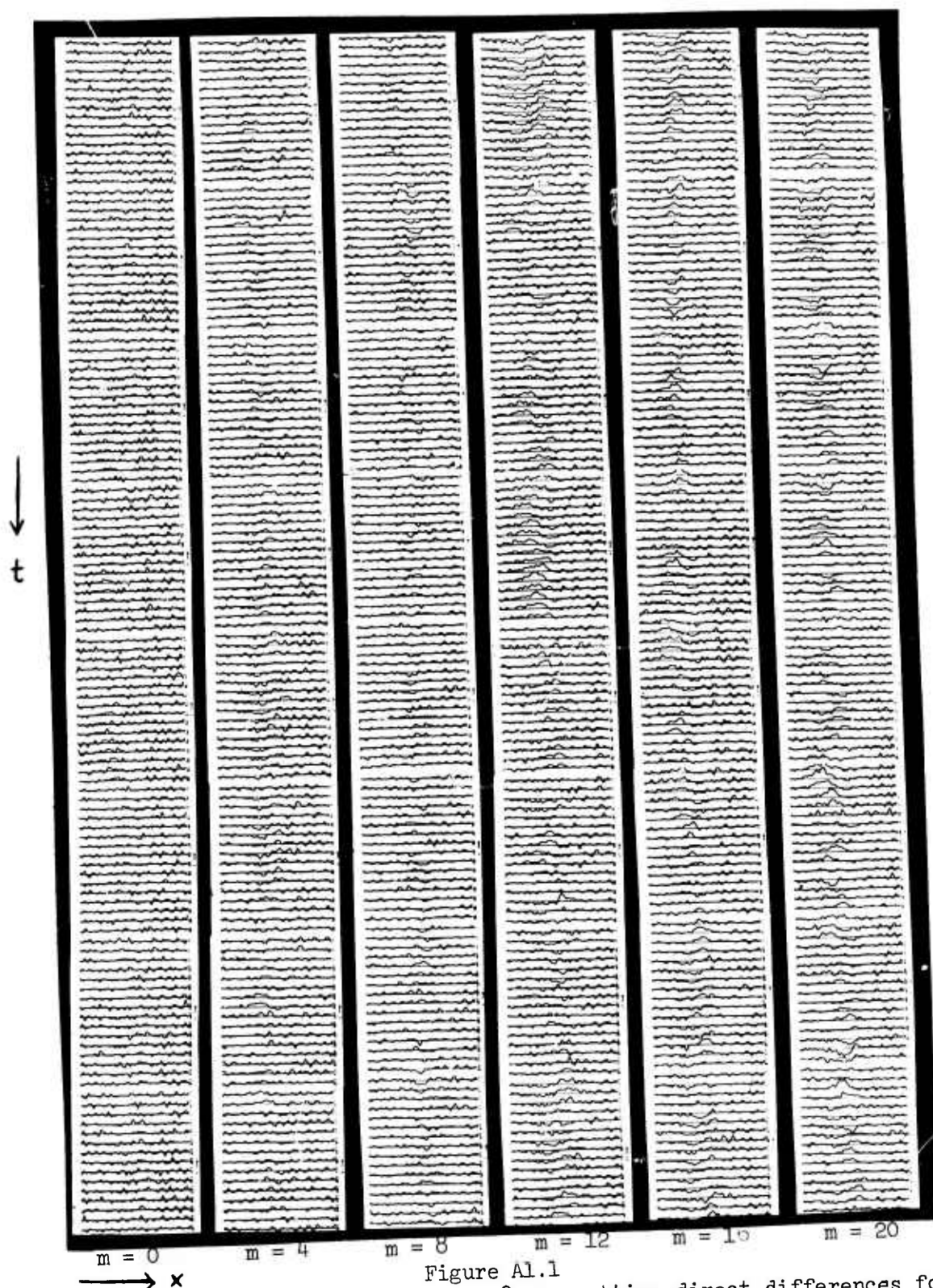


Figure A1.1
 Direct Differences - Each column is 128 consecutive direct differences for an array separation m (a separation of one unit is 0.5 arc seconds)

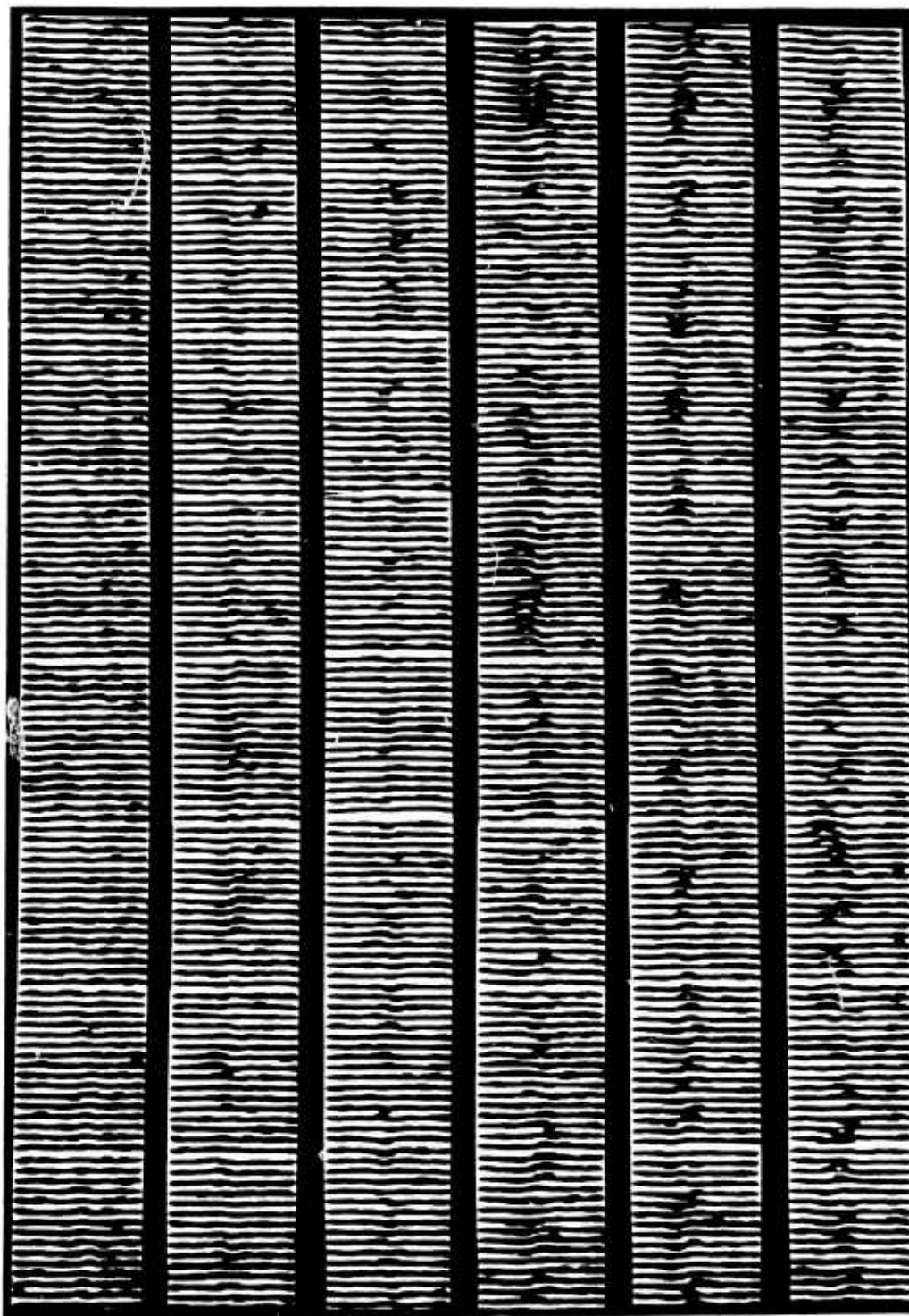


Figure A1.2

Defocused Direct Differences - This figure is A1.1 defocused and slid in the x direction to make variations clearer.

EXPERIMENT NUMBER 7 - SELF-PRODUCT

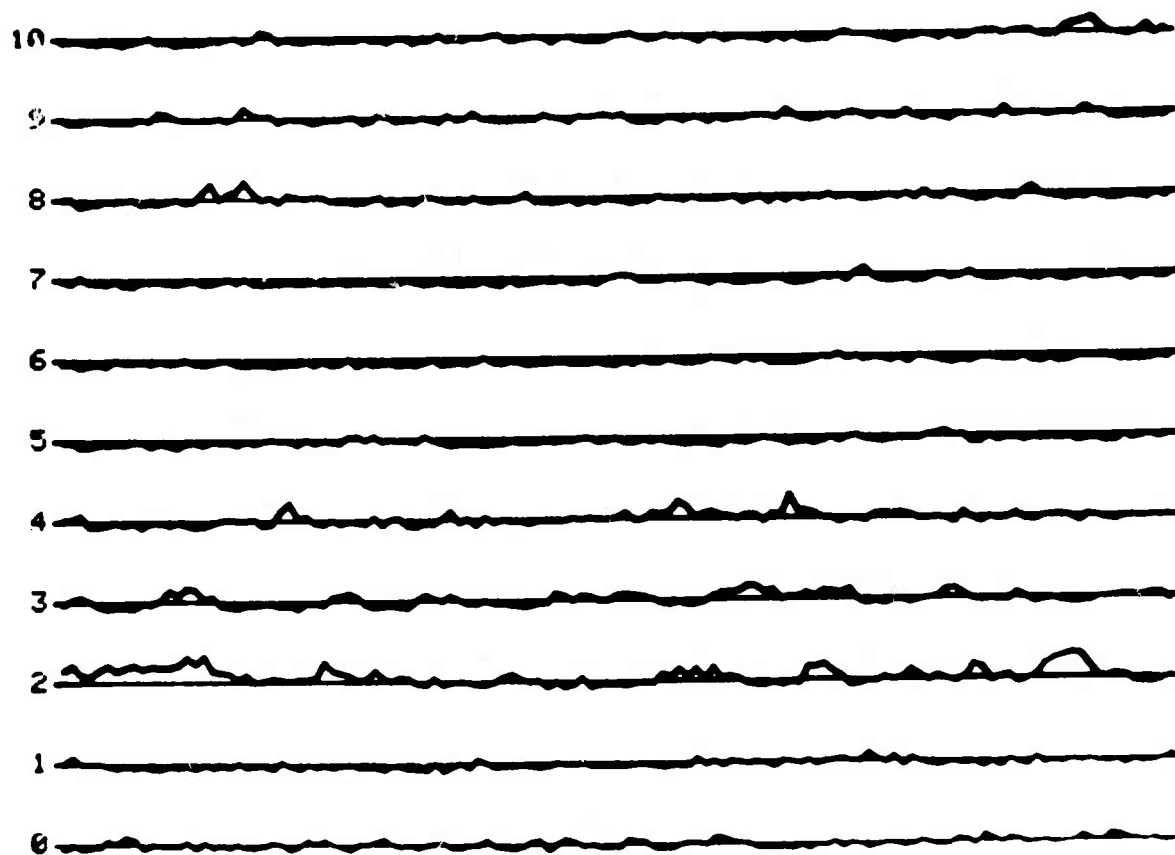


Figure A2.1

$\underline{D}_m^2(t)$ versus time for separations $m = 0$ to 10. Each time is labeled by the run number m . The separation between lines corresponds to a pure relative displacement of 0.7 arc seconds. The X (time) axis spans 128×12.5 milliseconds.

EXPERIMENT NUMBER 7 - SELF-PRODUCT

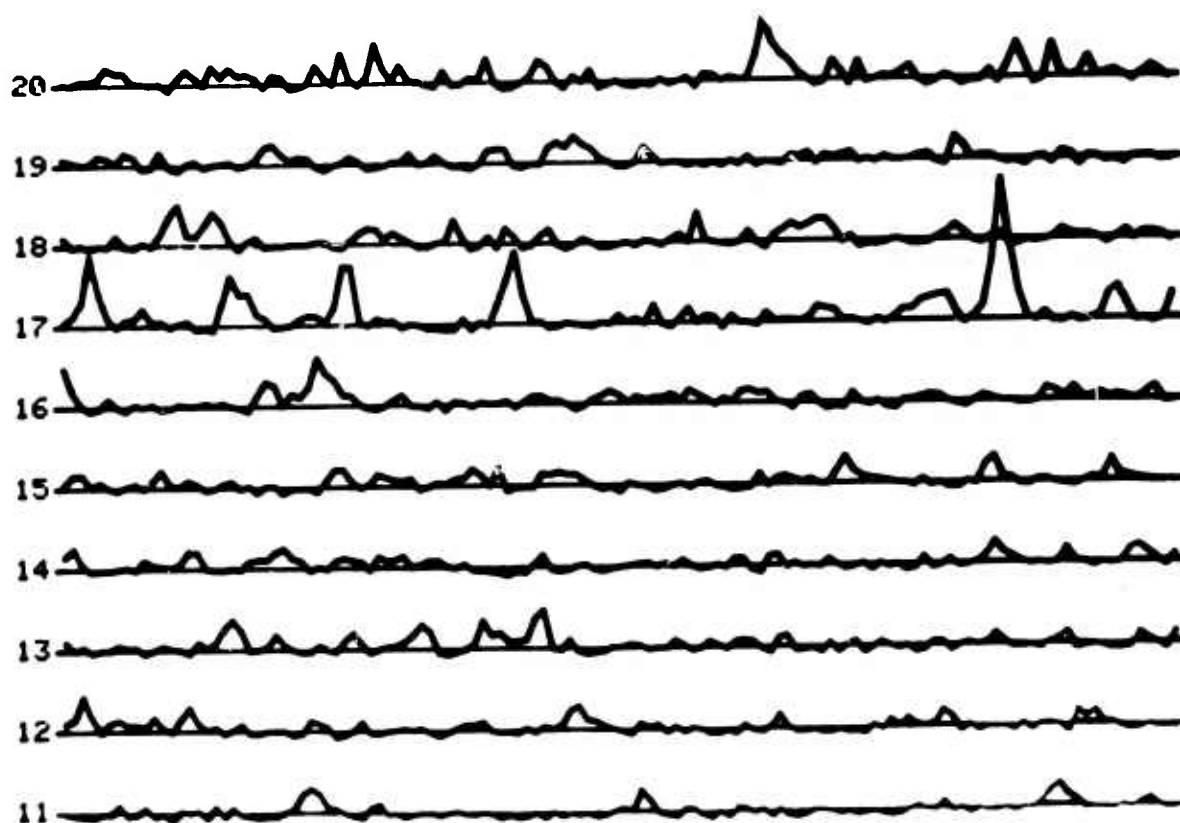


Figure A 2.2

$D_m^2(t)$ versus time for $m = 11$ to 20

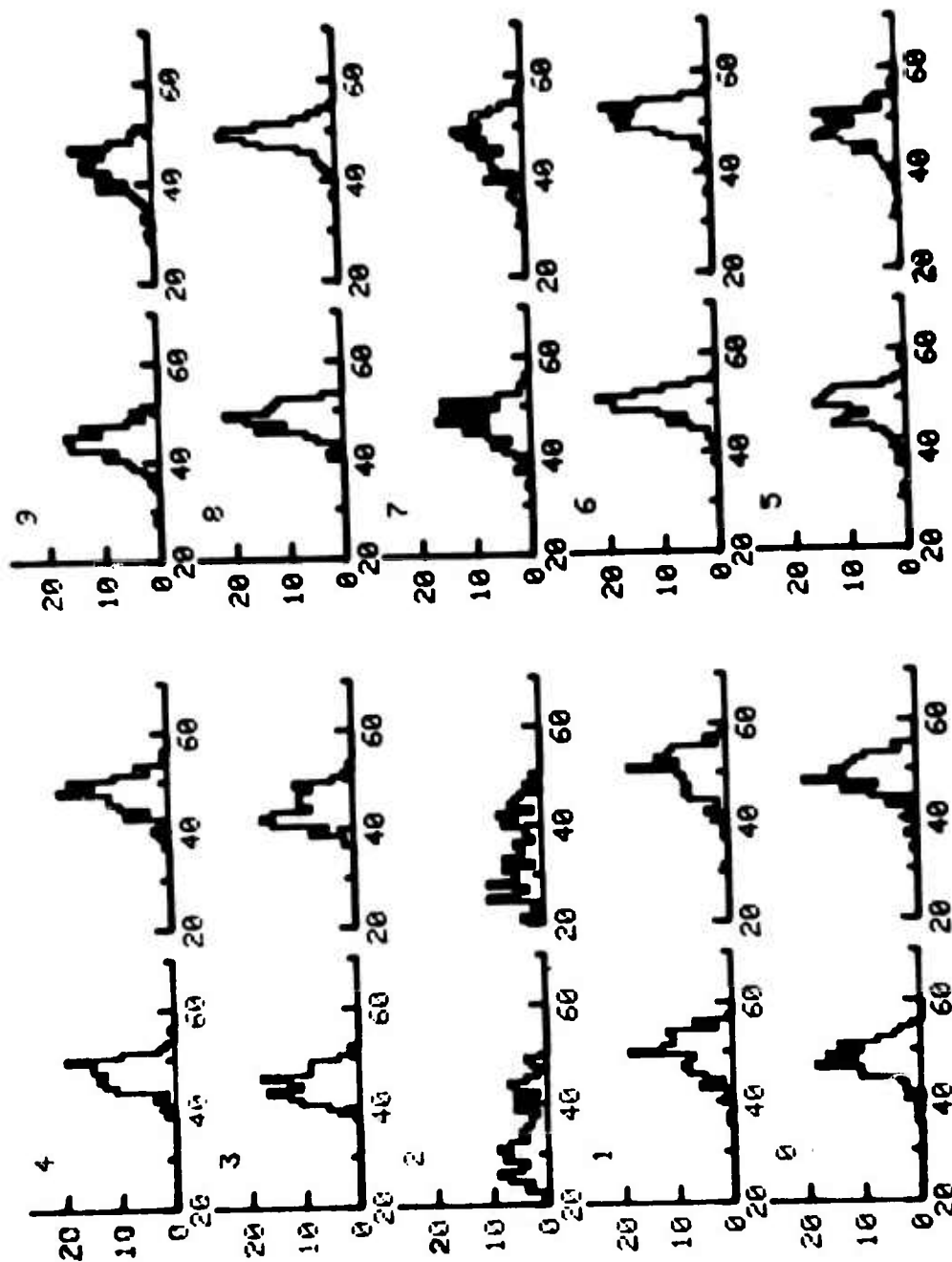


Figure A3.1

Number versus Slope for $m = 0$ to 9.
Histograms of the slope at limb center. A slope of 45 is the mean slope of the $m = 0$ run.

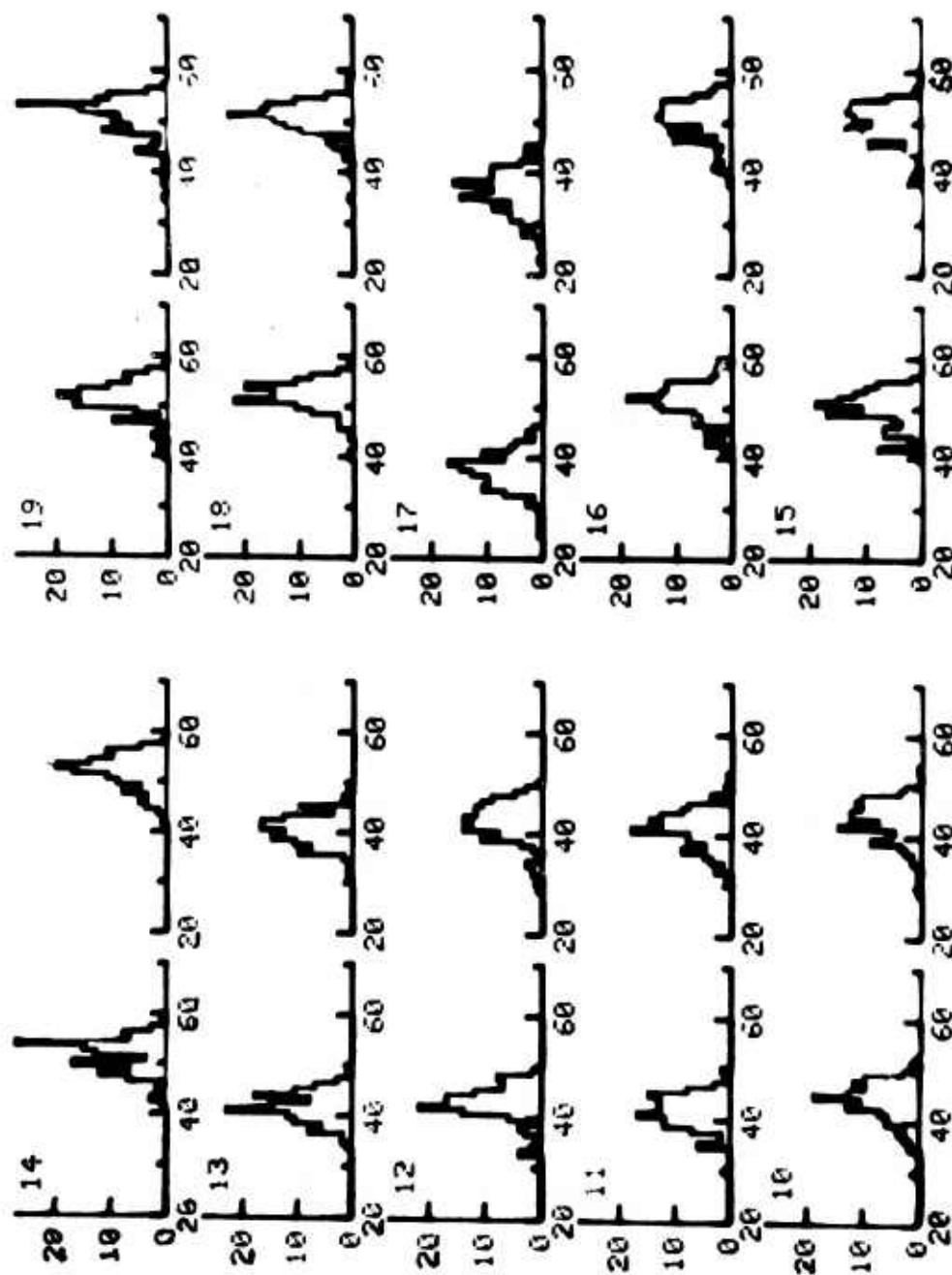


Figure A3.2

Number versus Slope for $m = 10$ to 19 .

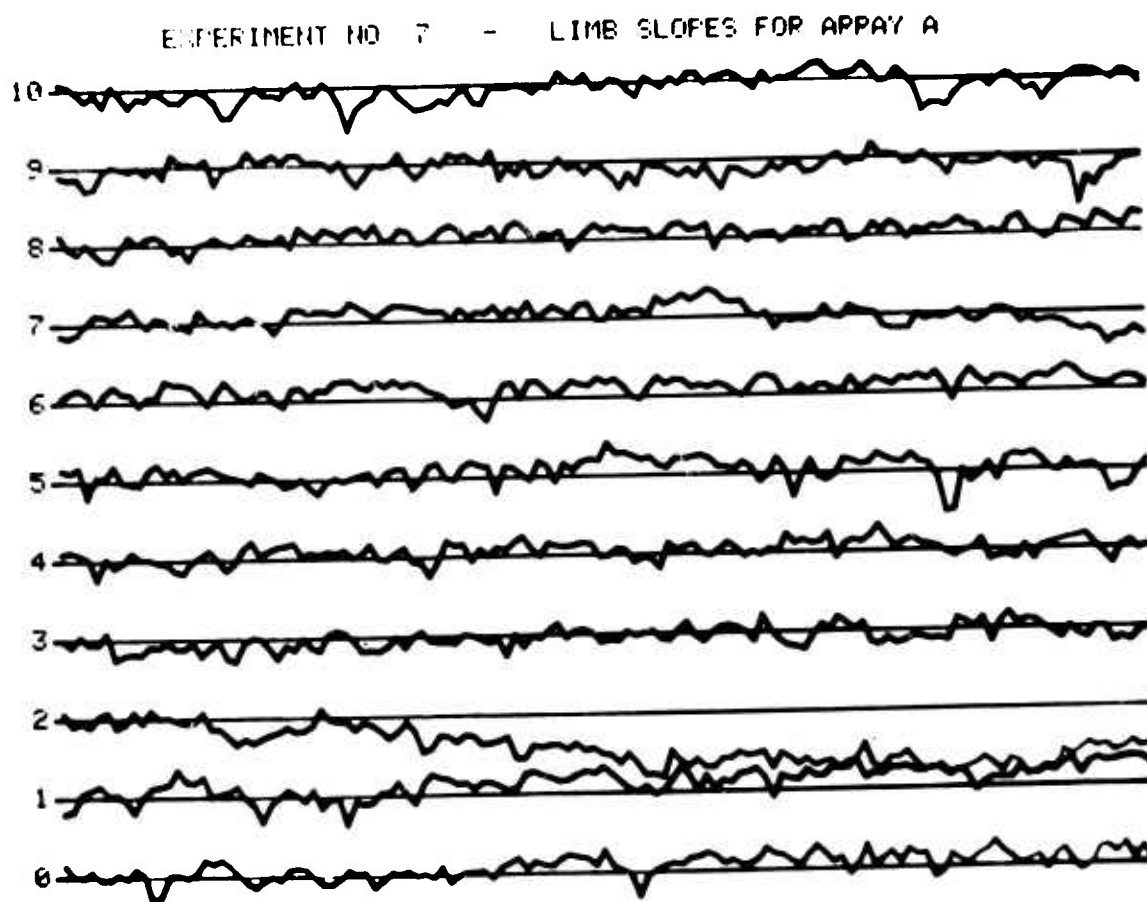


Figure A3.3
Slope versus time for $m = 0$ to 10.

The slope (y axis is auto-scaled). The purpose of the graph is to show the time history of the slope. Calibrated data is shown in A3.1 and A3.2.

ENTERMENT NO 7 - LIMB SLOPES FOR APPAY A

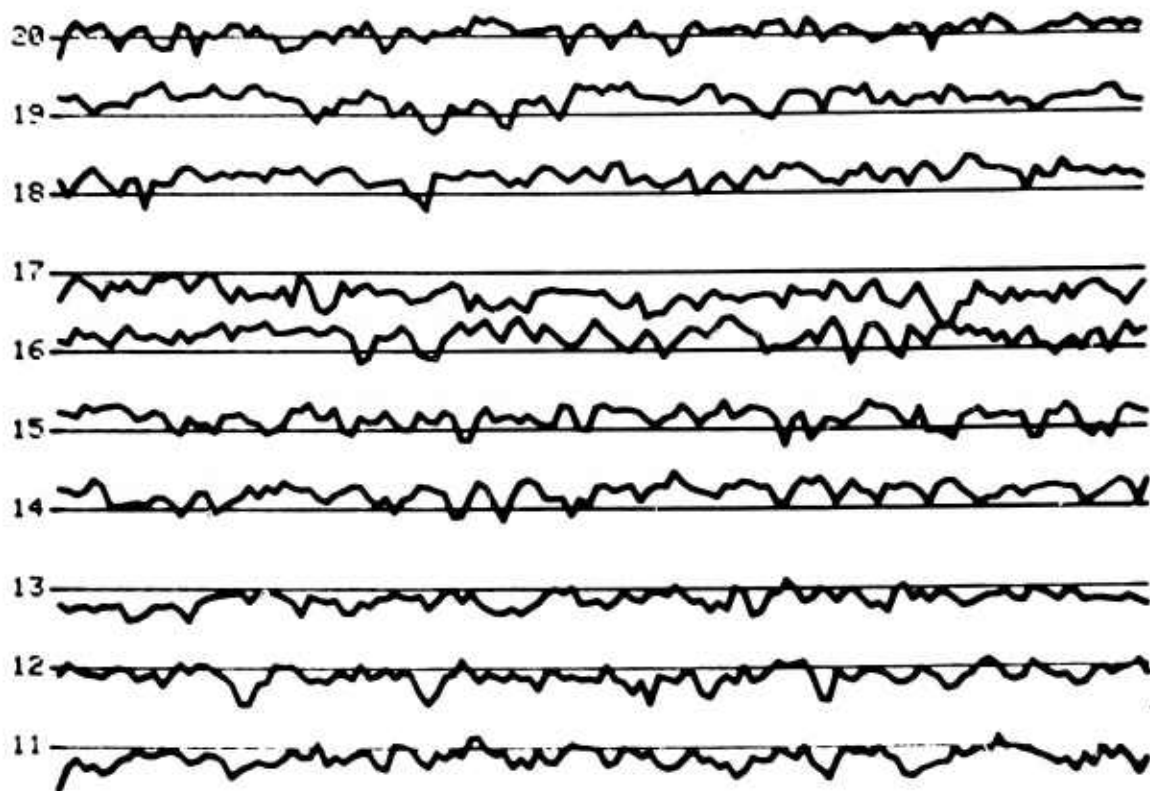


Figure A3.4

Slope versus time for $m = 11$ to 20.

EXPERIMENT NO 7

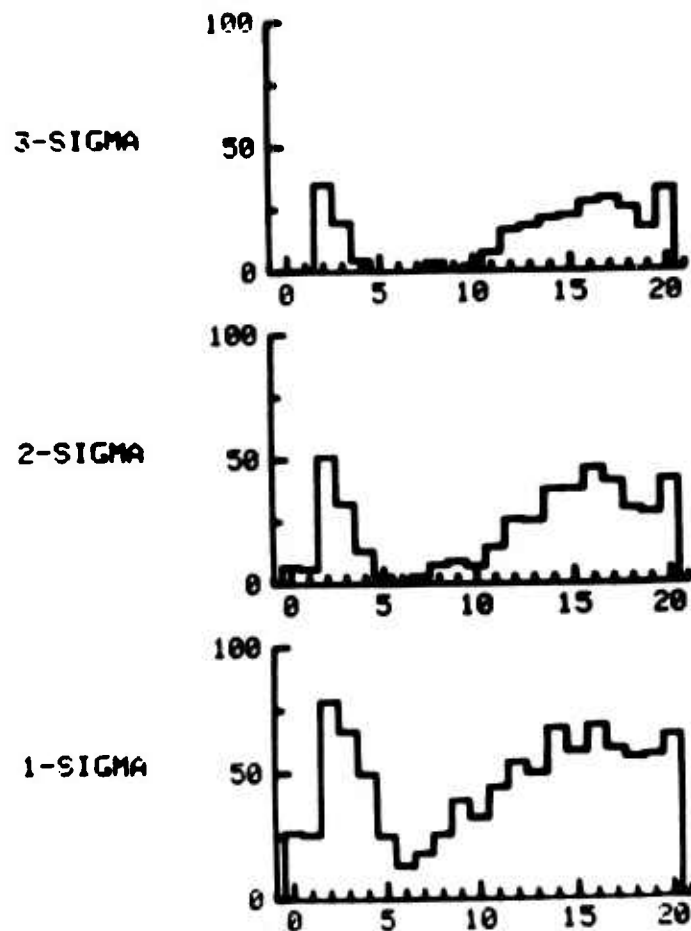


Figure 3.5
Histograms of the number of values of $D_m^2(t_k)$ greater than 1, 2 and 3 sigma versus m.

EXPERIMENT NUMBER 7 - CROSS PRODUCTS

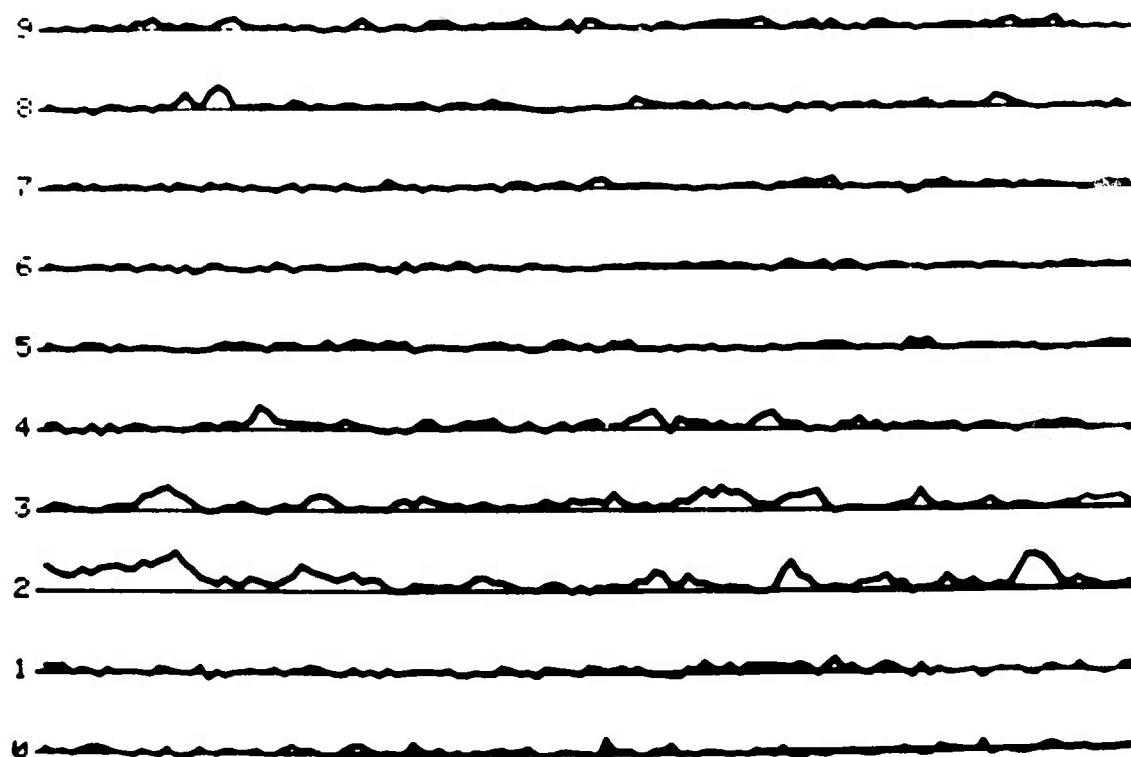


Figure A4.1
 $C_{p_m}(t,1)$ versus time $m = 0, 1$.

EXPERIMENT NUMBER 7 - CROSS PRODUCTS

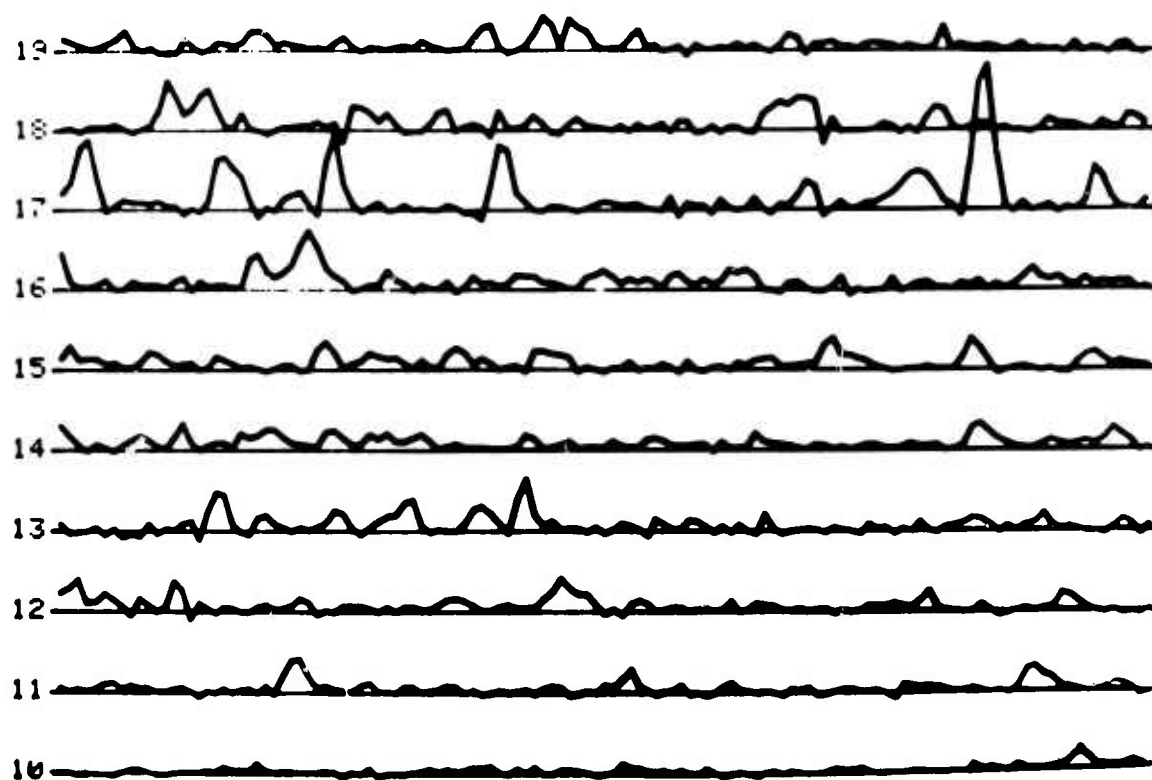


Figure A4.2
 $C_{P_m}(t,1)$ versus time $m = 11$ to 20.

EXPERIMENT NUMBER 7 - CROSS PRODUCTS (DELTA-T = 2)

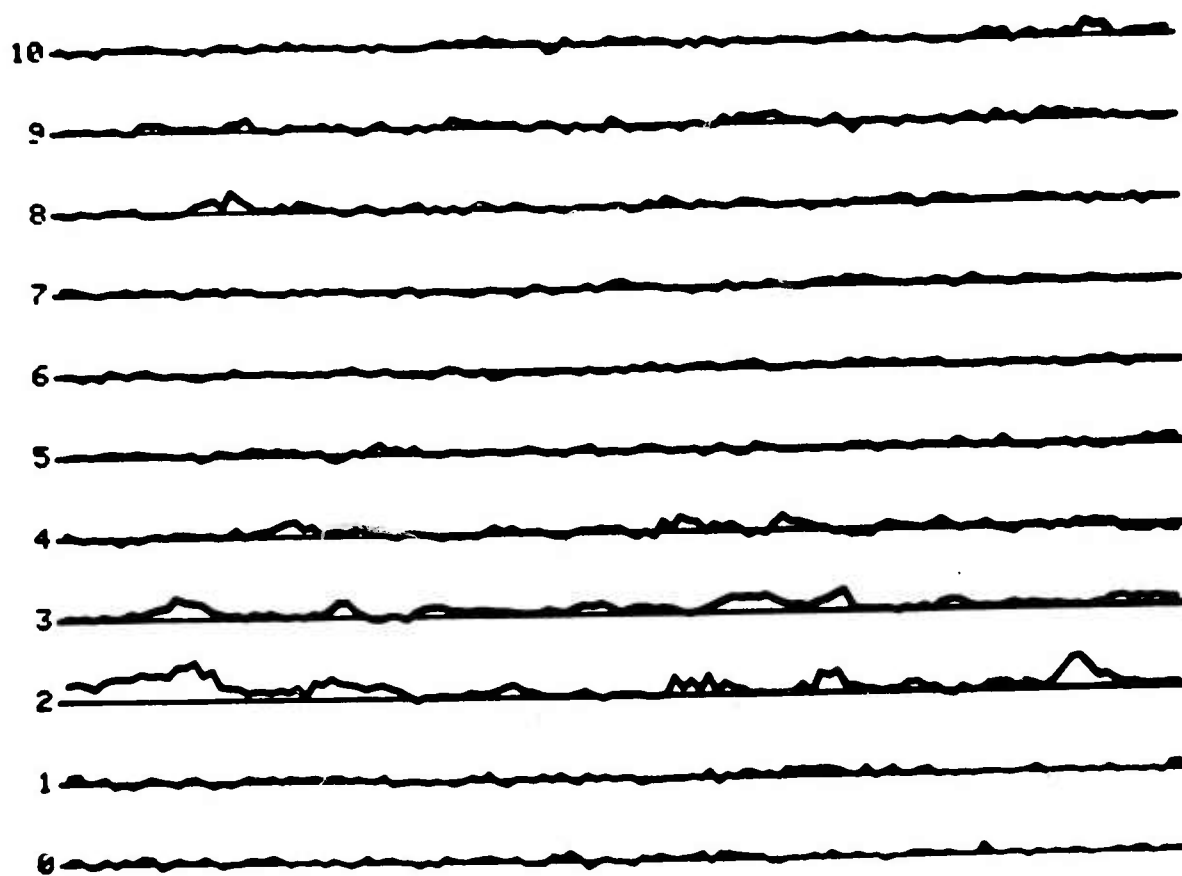


Figure A4.3

$C_{P_m}(t,2)$ versus time $m = 0, 10$

EXPERIMENT NUMBER 7 - CROSS PRODUCTS ($\Delta T = 2$)

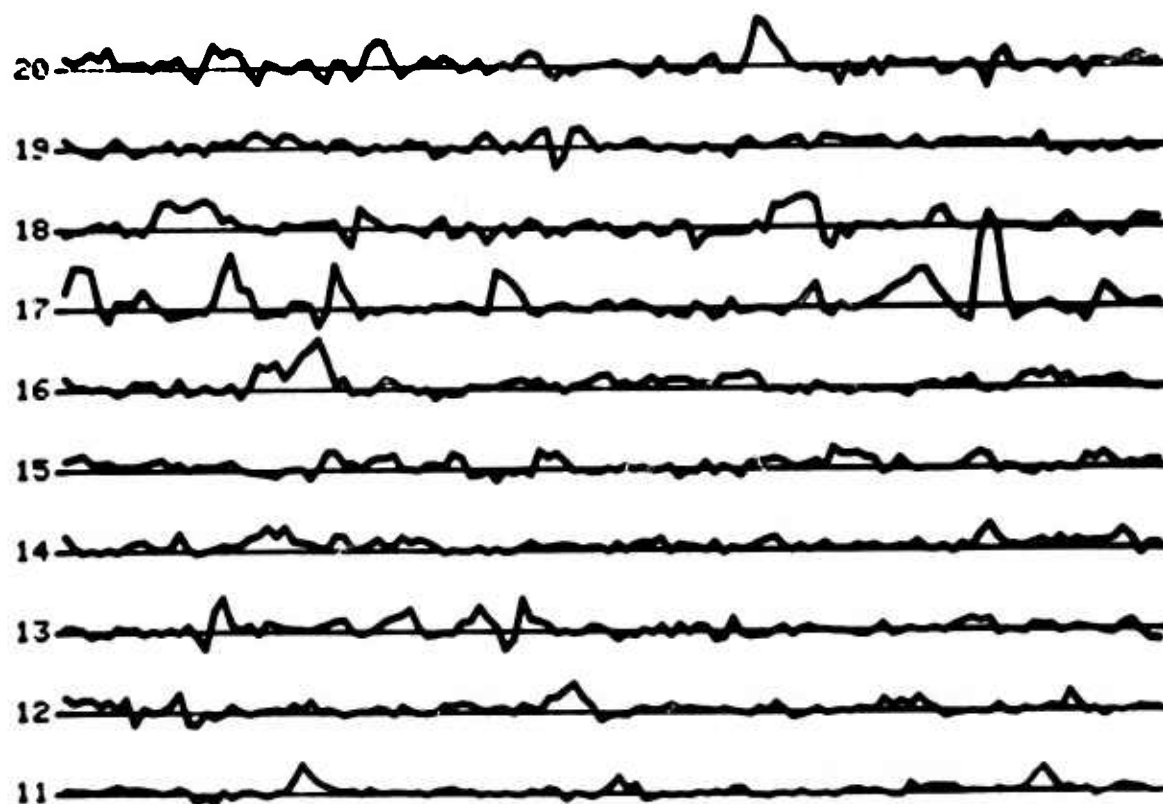


Figure A4.4
 $C_{P_m}(t, 2)$ versus time $m = 11$ to 20.

EXPERIMENT NUMBER 7 - CROSS PRODUCTS ($\Delta T = 4$)

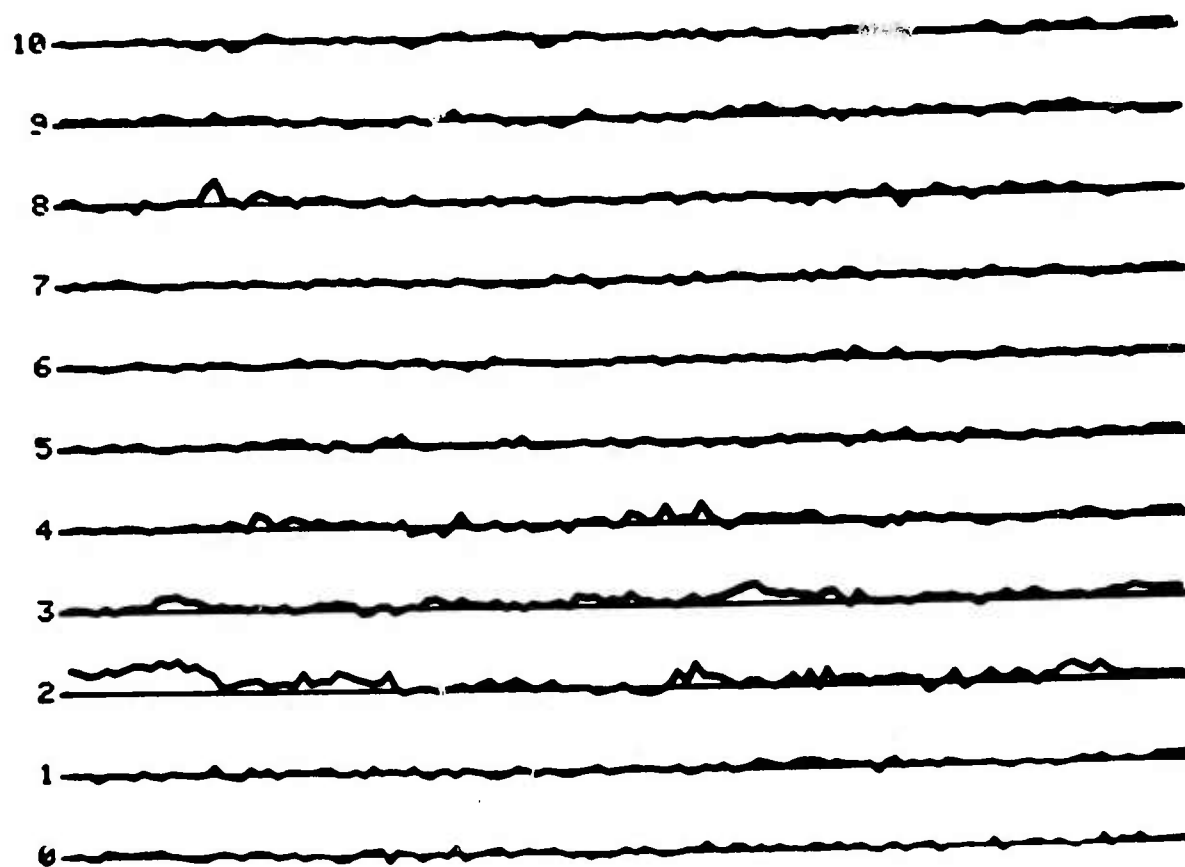


Figure A4.5
 $C_{P_m}(t, 4)$ versus time $m = 0, 10$.

EXPERIMENT NUMBER 7 - CROSS PRODUCTS (DELTA T = 4)

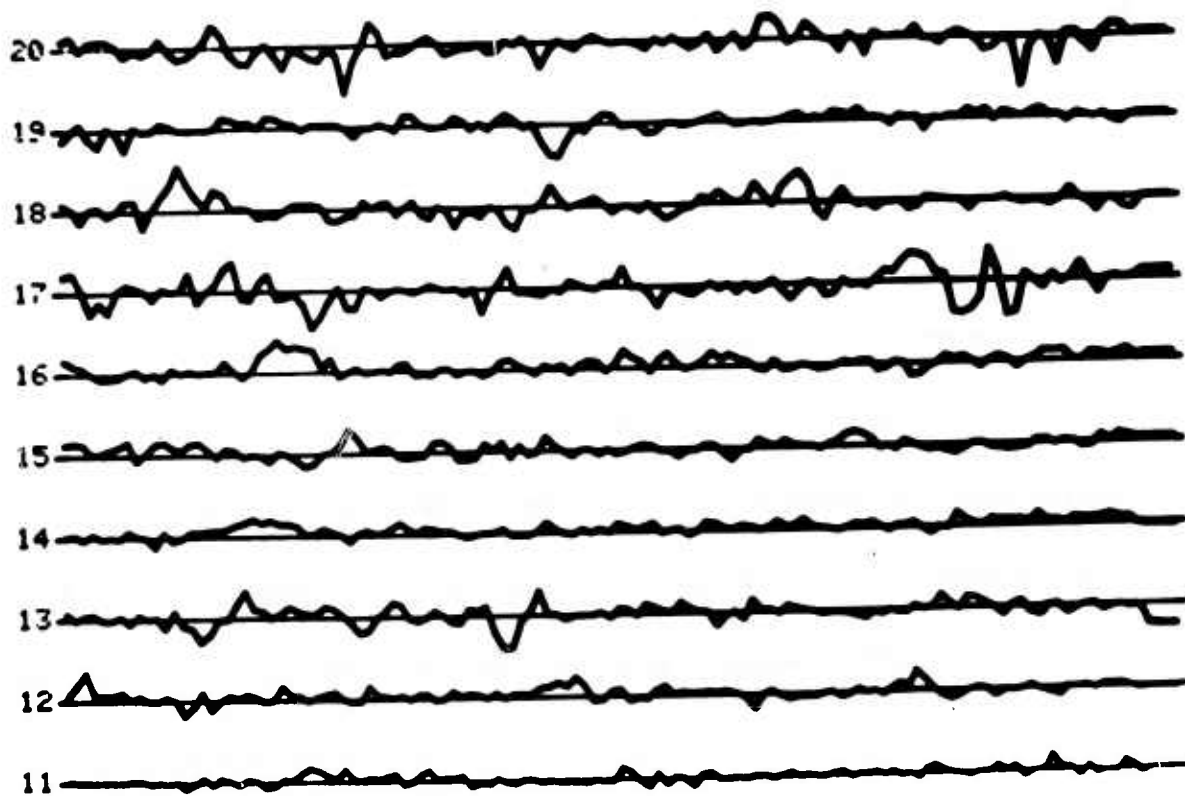


Figure A4.6
 $C_{P_m}(t, 4)$ versus time $m = 11, 20$.

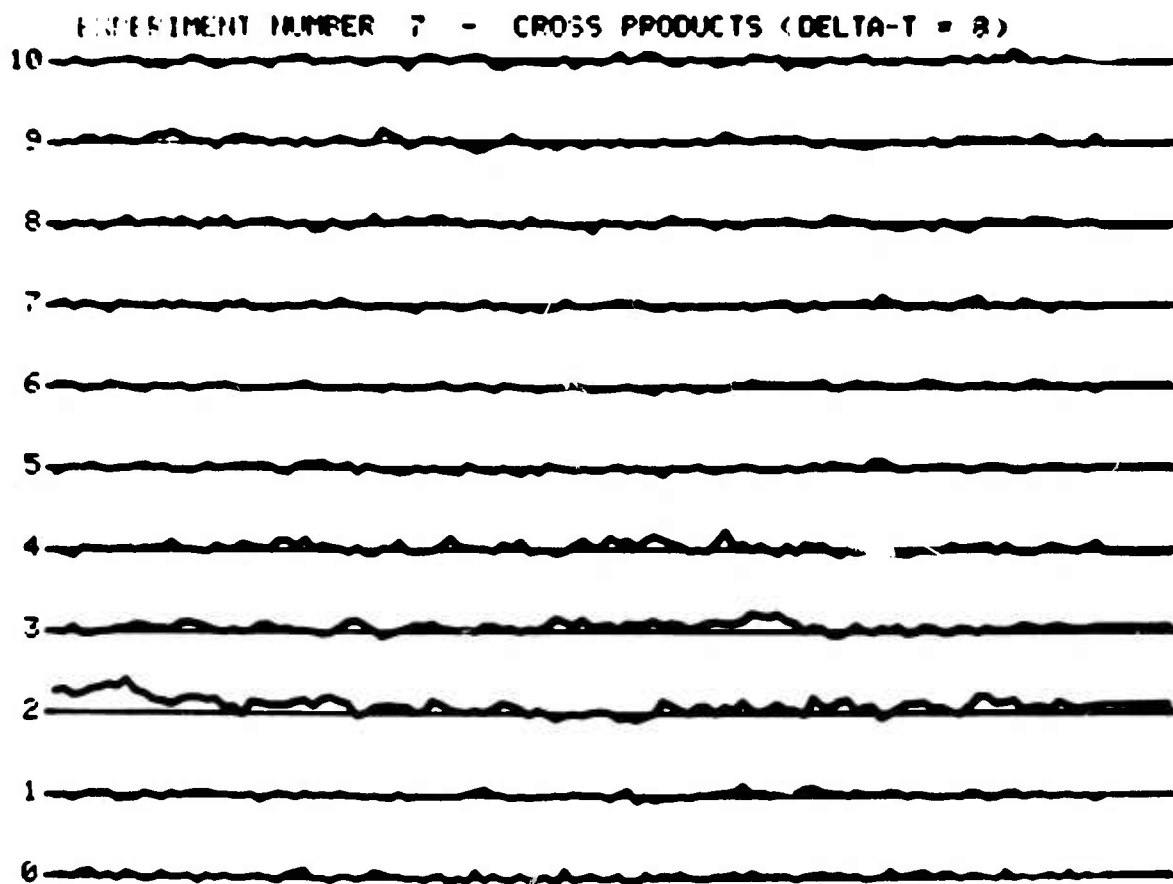


Figure A4.7
 $C_{P_m}(t, 8)$ versus time $m=0$ to 10.

EXPERIMENT NUMBER 7 - CROSS PRODUCTS (DELTA-T = 8)

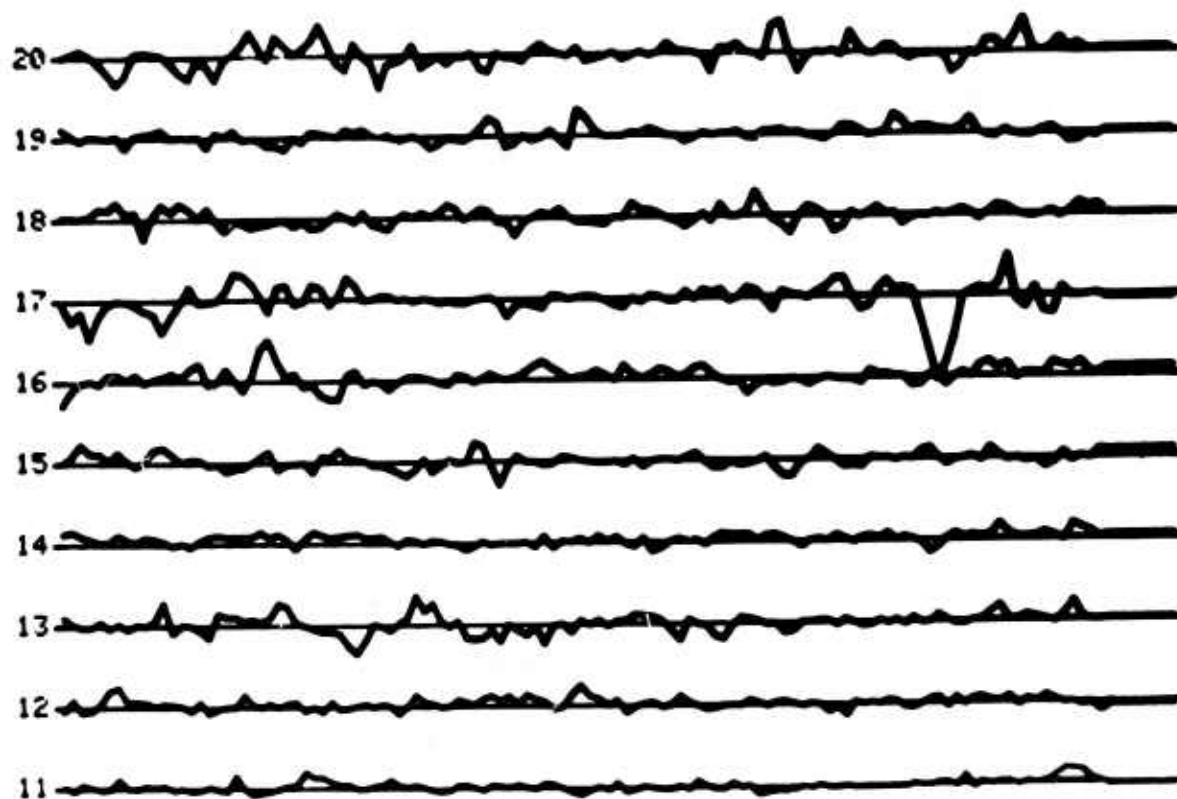


Figure A4.8
 $C_{P_m}(t, 8)$ versus time $m = 11$ to 20.

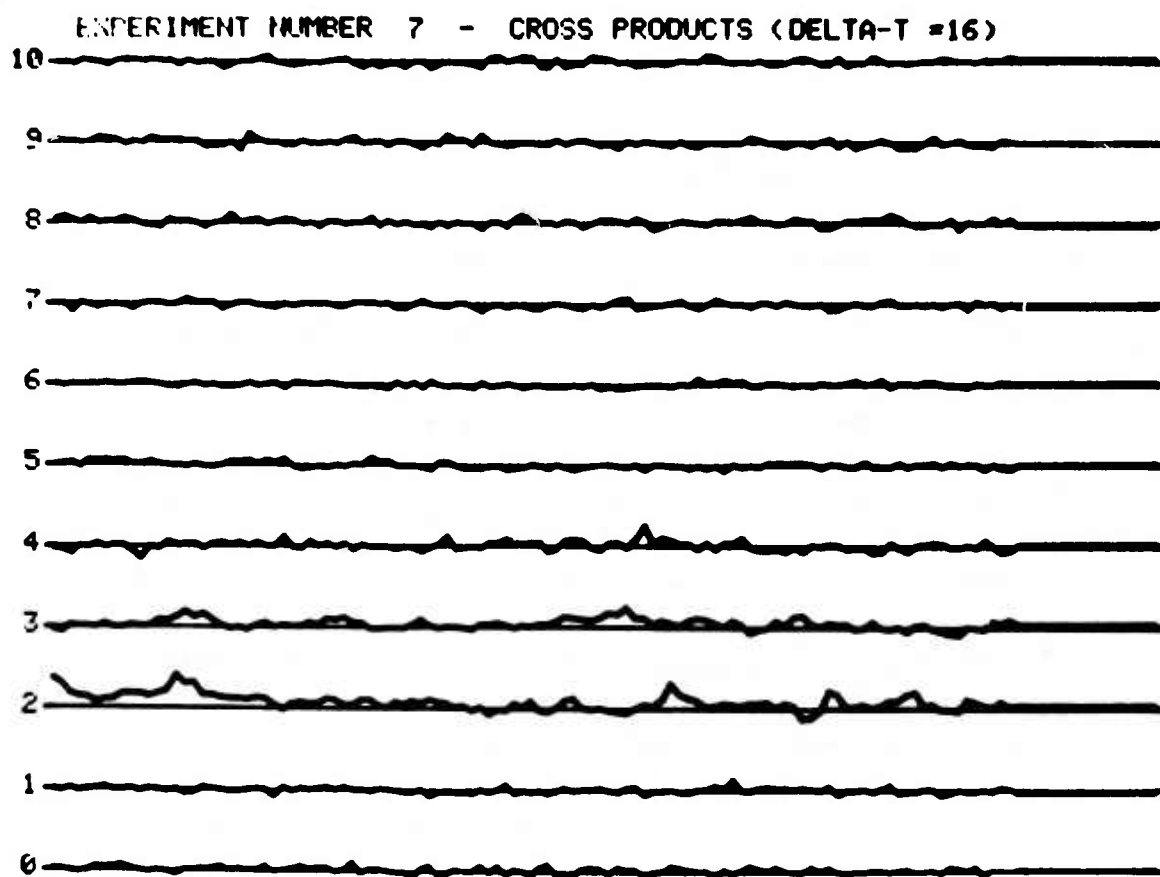


Figure A4.9

$C_{Pm}(t, 16)$ versus time $m = 0$ to 10.

EXPERIMENT NUMBER 7 - CROSS PRODUCTS (DELTA-T = 16)

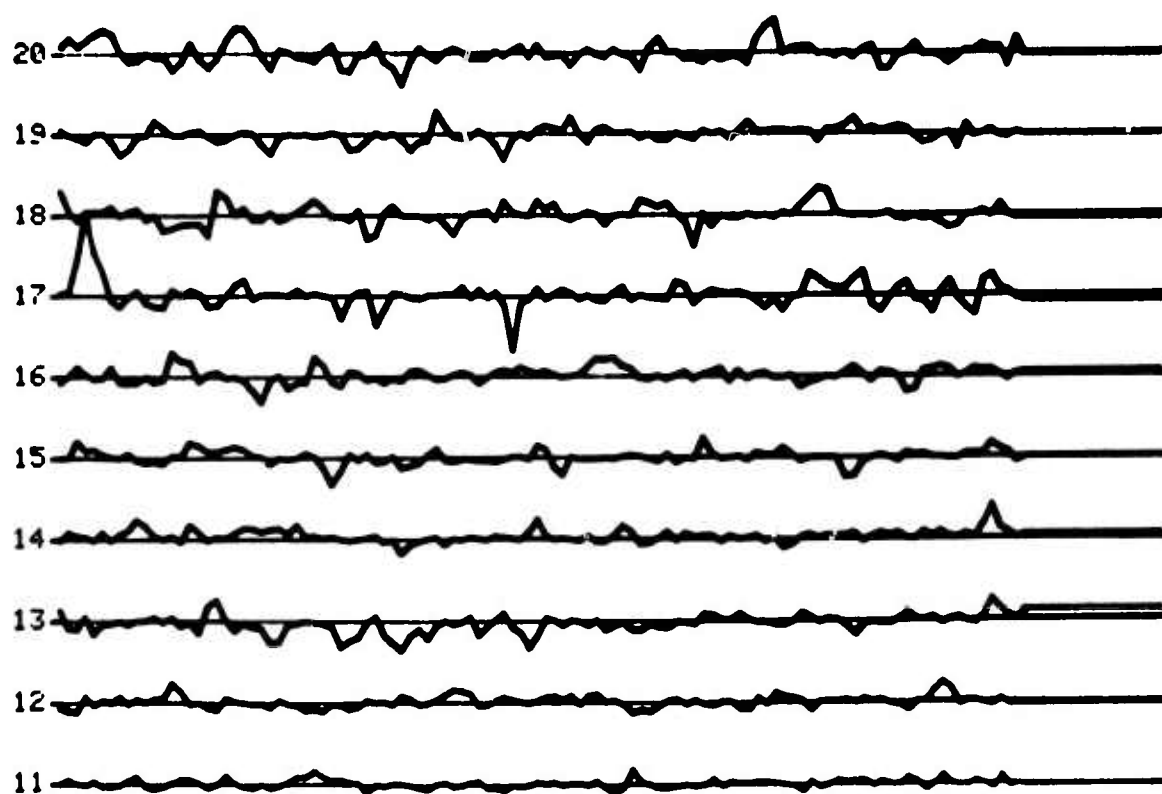


Figure A4.10

$C_{P_m}(t, 16)$ versus time $m = 11$ to 20.

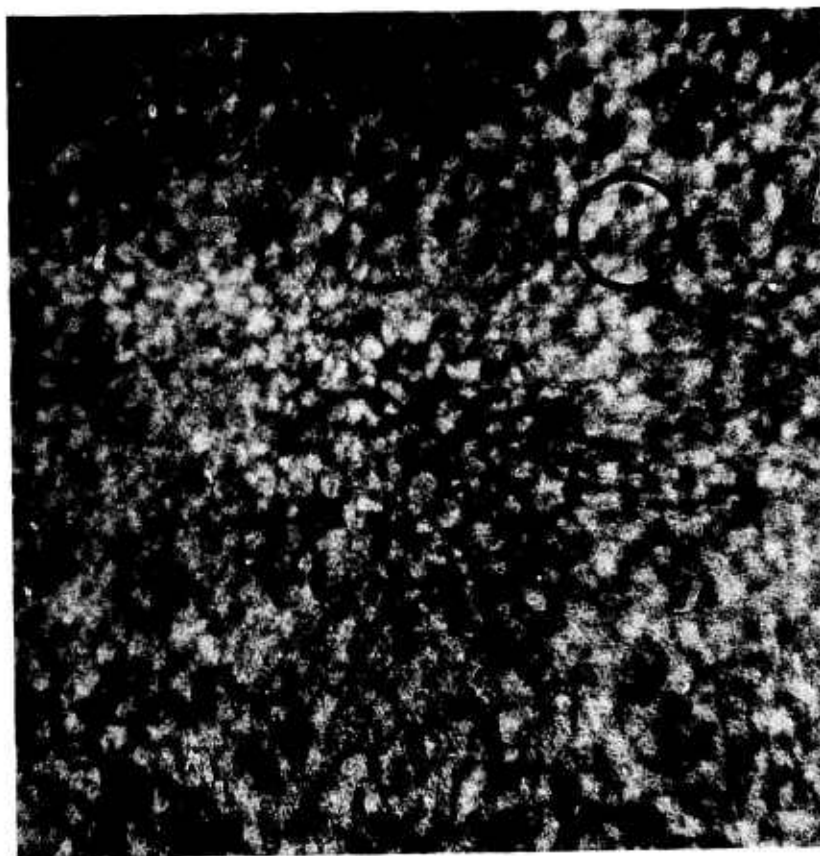


Figure A5.1
Photograph of the Sun with a 10 arc second comparison
circle.

MISSION of Rome Air Development Center

RADC is the principal AFSC organization charged with planning and executing the USAF exploratory and advanced development programs for information sciences, intelligence, command, control and communications technology, products and services oriented to the needs of the USAF. Primary RADC mission areas are communications, electromagnetic guidance and control, surveillance of ground and aerospace objects, intelligence data collection and handling, information system technology, and electronic reliability, maintainability and compatibility. RADC has mission responsibility as assigned by AFSC for demonstration and acquisition of selected subsystems and systems in the intelligence, mapping, charting, command, control and communications areas.

